

Boundary-layer receptivity of Mach 7.99 flow over a blunt cone to free-stream acoustic waves

By XIAOLIN ZHONG AND YANBAO MA

Mechanical and Aerospace Engineering Department, University of California, Los Angeles,
CA 90095, USA

(Received 27 February 2004 and in revised form 22 November 2004)

The receptivity phenomenon, which is the process of environmental disturbances initially entering the boundary layers and generating disturbance waves, is one of the important but not well understood mechanisms involving laminar–turbulent transition of hypersonic flows. This paper presents a numerical simulation study of the receptivity to weak free-stream fast acoustic waves for a Mach 7.99 axisymmetric flow over a 7° half-angle blunt cone. In hypersonic boundary-layer flow over a blunt cone, the process of receptivity to free-stream disturbances is altered considerably by the presence of a bow shock and an entropy layer. In the present study, both steady and unsteady flow solutions are obtained by computing the full Navier–Stokes equations with a fifth-order shock-fitting finite-difference scheme, which is able to account for the effects of bow-shock/free-stream-disturbance interaction accurately. The current numerical results for the steady base flow are compared with previous experimental and numerical results. In addition, a normal-mode linear stability analysis is used to identify the main components of boundary-layer disturbances generated by forcing free-stream fast acoustic waves. It is found that neither the first mode nor the second-mode instability waves are excited by free-stream fast acoustic waves in the early region along the cone surface, although the Mack modes can be unstable there. Instead, the second mode is excited downstream of the second-mode Branch I neutral stability point. The delay of the second-mode excitation is because the hypersonic boundary-layer receptivity is governed by a two-step resonant interaction process: (i) resonant interactions between the forcing waves and a stable boundary-layer wave mode I near the leading-edge region; and (ii) resonant interactions between the induced stable mode I and the unstable second Mack mode downstream. The same receptivity mechanism also explains the results that no first Mack mode components are generated by the current receptivity process because there is no resonant interaction between fast acoustic waves and the first Mack mode.

1. Introduction

The prediction of laminar–turbulent transition in hypersonic boundary layers is a critical part of the aerodynamic heating analyses on hypersonic vehicles. Despite decades of extensive research, the prediction of hypersonic boundary-layer transition is still mostly based on empirical correlation methods or the semi-empirical e^n method because a number of physical mechanisms leading to transition are currently not well understood. The receptivity phenomenon, which is the process of environmental disturbances initially entering the boundary layers and generating disturbance waves, is one of these important, but less understood, mechanisms. It is necessary to

understand the receptivity mechanisms in order to predict accurately the locations of transition. Though incompressible boundary-layer receptivity to free-stream disturbances is relatively well understood (Saric, Reed & Kerschen 2002), the process of hypersonic boundary-layer receptivity is much more complex (Morkovin 1987; Reshotko 1991) and is currently an active research area (Fedorov 2002, 2003; Fedorov & Khokhlov 2002; Ma & Zhong 2003*a, b*).

Most of our current knowledge on hypersonic boundary-layer stability and transition is based on the results of linear stability theory (LST) (Mack 1984), which is concerned with the linear growth or decay of boundary-layer normal modes. Mack (1984) showed that the stability characteristics of high supersonic and hypersonic boundary layers are very different from those of subsonic boundary layers. He found that, in addition to the first-mode instability waves, there are higher acoustic instability modes in hypersonic boundary layers. The unstable modes in hypersonic boundary layers are generally termed Mack modes in the literature. It was shown in Ma & Zhong (2003*a*) that the first, second and higher modes are in fact different segments of a single wave mode. Among the instability wave modes in hypersonic boundary layers, the second mode is the most dangerous in term of laminar–turbulent transition because it induces the dominant instability at hypersonic Mach numbers, especially for practical hypersonic flight applications where the free-stream disturbances are often very weak and the by-pass transition is not likely, and the second mode instability is a dominating instability before the transition of the boundary layers. The existence and dominance of the second mode instability in hypersonic boundary layers has been confirmed in experiments for hypersonic flows over sharp or blunt cones (Demetriades 1974, 1977; Stetson & Kimmel 1992; Maslov, Mironov & Shplyuk 2002).

The LST analysis is the foundation of the commonly used e^n method for boundary-layer transition prediction, which assumes that the transition is a result of exponential growth of the most unstable normal modes. For supersonic and hypersonic boundary-layer flows over a flat surface, the most unstable mode is the first Mack mode at relatively low Mach numbers and the second Mack mode for hypersonic boundary layers. The transition criteria used in the e^n method are established based on the ratio of amplitude growth of the most unstable mode computed by LST. The e^n method is a reasonable approach for practical hypersonic flight situations where environmental free-stream disturbances are small. However, the e^n method has the drawback that the initial generation of the unstable modes, which is the subject of a receptivity study, is not considered. Because the wave growth and transition in boundary layers depend on the initial amplitudes of the wave modes, the e^n transition prediction method without the consideration of the receptivity processes is not satisfactory. Therefore, an understanding of the mechanisms and characteristics of the receptivity process of hypersonic boundary layers is necessary in order to develop a better transition prediction method.

Stetson *et al.* (1984) and Stetson & Kimmel (1993) carried out boundary-layer stability experiments on an axisymmetric blunt cone in a Mach 7.99 free stream. The half angle of the cone was 7° , the nose radius was 3.81×10^{-3} m, and the free-stream Reynolds number based on the nose radius was 33 449. The total length of the cone was about 270 nose radii, corresponding to a Reynolds number of about 9 million. Detailed fluctuation spectra of the disturbance waves developing along the body surface were measured in the experiments. It was found that the disturbances in the boundary layer were dominated by the second mode instability. Significant superharmonic components of the second modes were observed after the second mode became dominant. Compared with similar hypersonic flow over a sharp cone,

the second mode instability of the blunt cone appeared in much further downstream locations. This indicates a stabilization of the boundary layer by slight nose bluntness. Stetson and colleagues also found evidence of entropy-layer instability in the region outside the boundary layer in a test case of larger nose radius. This particular stability experiment was identified by NATO RTO Working Group 10 on boundary layer transition (Schneider 2001) as one of the best available stability experiments for computational fluid dynamics (CFD) code validation.

Stability experiments of hypersonic flows over sharp or blunt cones have also been carried out by other workers. Demetriades (1974, 1977) carried out extensive stability experiments on hypersonic boundary layers over axisymmetric cones. He presented detailed disturbance spectra in the boundary layers and obtained visualization of the laminar rope waves, which are the signature of the second mode waves in the hypersonic boundary layers.

Maslov and his colleagues (2001, 2002) reported their stability experiments on supersonic and hypersonic flows over sharp or blunt cones. One of the test cases was Mach 5.92 flow over a 7° half-angle blunt cone, which had similar geometry and flow conditions to those tested in Stetson *et al.*'s 7° blunt cone experiments. Maslov *et al.* measured the fluctuation spectra of the disturbance waves in the boundary layer for test cases of instability waves induced by two different mechanisms: (i) natural disturbances in the wind tunnel; and (ii) artificial disturbances introduced into the boundary layer by high-frequency glow discharge on the cone surface. They found that, in the case of a sharp cone without artificial forcing disturbances, the disturbance waves in the boundary layer at the measurement location are dominated by the second mode waves. On the other hand, for the case of the blunt cone, the first mode disturbances have smaller amplitudes and the second mode disturbances are practically absent. They also found that when the disturbances are induced by glow discharge on an early part of the cone surface, the amplification of the disturbances is similar for both the blunt and the sharp cones, i.e. they are mainly the second mode waves for both cases. They conjectured that the considerable difference in the case of natural disturbances is caused by different receptivity conditions and by the development of the disturbances at low Reynolds numbers on the sharp and blunt cones.

The normal-mode linear stability characteristics of the boundary-layer flow over the same blunt cone as Stetson *et al.*'s experiments have been studied by a number of workers (Malik, Spall & Chang 1990; Herbert & Esfahanian 1993; Kufner, Dallmann & Stilla 1993; Kufner & Dallmann 1994). Malik *et al.* (1990) computed the neutral stability curve and compared the growth rates obtained by LST with the experimental results. The steady base flow solution was computed by using the parabolized Navier–Stokes equations. They found that the nose bluntness stabilizes the boundary layer. The growth rates predicted by the LST were compared with Stetson *et al.*'s experimental results at the surface location of $s = 175$ nose radii. The linear stability analyses predicted slightly lower frequency for the dominant second mode, but much higher amplification rates than the experimental results. Herbert & Esfahanian (1993) conducted similar base flow and LST calculations for the same Mach 7.99 flow by using a much finer grid resolution. Their LST results at the $s = 175$ surface station agree reasonably well with those of Malik *et al.* In a separate study, Kufner *et al.* (1993) and Kufner & Dallmann (1994) carried out extensive LST calculations for the same flow over the blunt cone. It was found that there are only small variations in the LST growth rates obtained independently by the three group of authors. The small variations among these three sets of LST growth rates are possibly caused by differences in their mean flow solutions. However, all LST results consistently

predicted much higher growth rates than those of the stability experiments at the 175 nose radii surface station. A satisfactory explanation for the growth-rate discrepancy between the LST and experimental results has not been found. It has been speculated that the discrepancy is a result of the nonlinear effects in the experimental wave fields because there are significant superharmonic components at the 175 nose radii station in the experimental results. On the other hand, the nonlinear effects are neglected in the linear stability analysis. Other factors may also be responsible for the discrepancy. For example, the effects of bow shock, entropy layer, and non-parallel boundary layer are neglected in the normal mode linear stability analysis. Since these complex physical effects and interactions neglected by theoretical analyses are taken into account in a direct numerical simulation of the full Navier–Stokes equations, direct numerical simulation studies of the stability and receptivity will not only be a useful research tool in understanding new hypersonic boundary stability mechanisms, but also be helpful in evaluating the accuracy of LST results for hypersonic boundary-layer stability.

The direct numerical simulation of hypersonic and supersonic boundary-layer receptivity was carried out in our previous studies (Ma & Zhong 2001, 2002, 2003*a–c*). A parametric study was carried out on the receptivity characteristics affected by different free-stream waves, frequencies, nose bluntness characterized by Strouhal numbers, Reynolds numbers, Mach numbers and wall cooling (Zhong 1997*a*, 2001). It was found that the receptivity parameters decrease when the forcing frequencies or nose bluntness increase. The mechanisms of the receptivity of supersonic flat-plate boundary layer to free-stream fast acoustic waves were studied by using both direct numerical simulation and the LST (Ma & Zhong 2001, 2002, 2003*a, b*). The results showed that the receptivity of the flat-plate supersonic boundary layer to free-stream fast acoustic waves leads to the excitation of both Mack modes and a family of stable modes, which were termed mode I, mode II, etc. by Ma & Zhong. The receptivity characteristics of supersonic boundary layers were found to be very different from those of the incompressible counterpart owing to a different length scale between the free-stream forcing waves and Tollmien–Schlichting (T-S) waves (Saric *et al.* 2002). Specifically, at low Mach number, the differences between the wavelengths of the acoustic waves and instability waves require a change in curvature on a surface as a wavelength matching point. At supersonic Mach numbers, the wavelength matching mechanism is not necessary. Therefore at high Mach numbers, interaction between acoustic and vortical waves can occur anywhere in the flow. It was found that the forcing fast acoustic waves do not interact directly with the unstable Mack modes in supersonic boundary layers. Instead, the stable mode I waves play an important role in the receptivity process because they interact with both the forcing fast acoustic waves and the unstable Mack-mode waves. Through these interactions, the stable mode I waves transfer disturbance energy from the forcing fast acoustic waves to the second Mack-mode waves. The results also showed that the receptivity mechanisms of the second mode are very different from those of modes I and II. The different mechanisms between the second mode and mode I (or mode II) lead to different responses to different incident wave angles, frequencies and wall boundary conditions.

Ma & Zhong (2003*c*) subsequently carried out numerical simulations of the receptivity to free-stream disturbances of Mach 7.99 flow over a 5.3° sharp wedge. The free-stream disturbances included fast acoustic, slow acoustic, entropy and vorticity waves. It was found that, similar to the flat-plate case, the stable mode I waves play an important role in the receptivity process because they interact with both the forcing acoustic waves and the unstable Mack modes. On the other hand, the forcing slow

acoustic waves can directly generate Mack-mode waves because of their resonant interactions. At small incident angles, slow acoustic waves are more efficient in generating the unstable second Mack modes than the fast acoustic waves. For receptivity to free-stream entropy waves or vorticity waves, the generation of boundary-layer disturbances are mainly through fast acoustic waves generated behind the shock due to the interactions between shock waves and free-stream disturbances. These extensive DNS studies have produced clear pictures of the mechanisms of the receptivity of supersonic and hypersonic boundary layers.

The results of the numerical simulation studies of Ma & Zhong (2002, 2003*a–c*) are consistent with the theoretical analysis of the receptivity of hypersonic boundary layers by Fedorov & Tumin (2001), Fedorov & Khokhlov (2001, 2002) and Fedorov (2002, 2003). Fedorov and colleagues found that the disturbance spectra reveal the following features: (i) the mode I and Mack modes are synchronized with fast and slow acoustic waves near the leading edge; (ii) further downstream, mode I is synchronized with entropy and vorticity waves; (iii) near the lower neutral branch of the Mack second mode, mode I is synchronized with the Mack second mode.

The previous numerical studies of Ma & Zhong (2001, 2002, 2003*a–c*) and theoretical studies of Fedorov and colleagues on high-speed boundary-layer receptivity have been for supersonic or hypersonic flows over sharp flat plates or wedges only. The effects of nose bluntness and entropy layers on receptivity were not considered in these studies. In hypersonic boundary-layer flow involving a blunt nose, the receptivity to free-stream disturbances is altered considerably by the presence of a bow shock and an entropy layer created by the blunt nose. Before entering the boundary layer, free-stream disturbances first pass through and interact with the bow shock. Irrespective of the nature of a free-stream disturbance waves, their interaction with the bow shock always generates all three types of disturbance wave after passing through the shock. These three types of wave are acoustic, entropy and vorticity waves. The transmitted waves are propagated downstream and interact with the boundary layer near the body. On the other hand, an entropy layer is created by the bow shock and gradually merges with the boundary layer as it is convected downstream. In the stability experiments of Stetson *et al.* (1984), evidence of entropy-layer instability was observed in the region outside the boundary layer for a test case with a blunt cone of larger nose radius.

This paper presents a numerical study on the receptivity to free-stream acoustic waves for hypersonic flow with the effects of nose bluntness and the entropy layer. The flow conditions duplicate the experiments of Stetson *et al.* (1984) and aim to investigate new physics in high-Mach-number flows that can lead to transition, and thereby motivate new experiments. The numerical results are compared with available experimental and other computational results. More importantly, the detailed receptivity and stability mechanisms are studied by numerical simulation. The effects of nose bluntness, entropy layer, shock-disturbance interaction, non-parallel boundary layers and surface curvature on the receptivity process are accurately taken into account by the high-order shock-fitting scheme. Whenever possible, the current numerical results are compared with those of the experiments by Stetson *et al.* and with the numerical simulation results by Herbert & Esfahanian (1993). In addition, a new axisymmetric LST code is developed to study the linear stability and receptivity properties of the axisymmetric boundary layer. The new axisymmetric LST code is validated by comparing its results with the other LST results on the same flow field. Subsequently, the LST results are used to identify and analyse the wave structures and interactions based on the simulation results. From the analyses of the simulation

results, we study the hypersonic boundary-layer receptivity mechanisms, and the corresponding effects from nose bluntness and the entropy layer. In addition, the second-mode growth rates obtained by the linear stability analysis are also compared with those of the numerical simulation as a first step in explaining the discrepancy between the experimental and LST growth rates.

2. Governing equations and numerical methods

The governing equations for both steady and unsteady flow computations are briefly presented in this section. Details of the governing equations and numerical methods for two- and three-dimensional flows have been described in previous papers (Zhong 1997*a, b*). The governing equations are the unsteady three-dimensional Navier–Stokes equations written in the following conservation-law form:

$$\frac{\partial U^*}{\partial t^*} + \frac{\partial F_j^*}{\partial x_j^*} + \frac{\partial F_{vj}^*}{\partial x_j^*} = 0, \quad (1)$$

where $U^* = (\rho^*, \rho^* u_1^*, \rho^* u_2^*, \rho^* u_3^*, e^*)$, and superscript ‘*’ represents dimensional variables. The Cartesian coordinates, (x^*, y^*, z^*) , are represented by (x_1^*, x_2^*, x_3^*) in tensor notation. In the current simulation of axisymmetric flow over a blunt cone, the x^* -axis is along the centre line of the axisymmetric cone pointing downstream. The origin of the Cartesian coordinate system is located at the centre of the spherical nose.

We non-dimensionalize the flow velocities by the free-stream velocity U_∞^* , length scales by the nose radius r_n^* , density by ρ_∞^* , pressure by p_∞^* , temperature by T_∞^* , time by r_n^*/U_∞^* , etc. The dimensionless flow variables are denoted by the same dimensional notation, but without the superscript ‘*’.

A fifth-order shock-fitting method of Zhong (1998) is used to compute the flow field bounded by the bow shock and wall surface. The flow variables behind the shock are determined by the Rankine–Hugoniot relations across the shock and a characteristic compatibility equation from behind the shock. The details of the shock-fitting formulae and numerical methods can be found in Zhong (1998).

3. Flow conditions

The flow conditions for the test case studied in this paper are the same as those of Stetson *et al.*’s (1984) experiments on air flow over a blunt cone. The specific flow conditions are:

$$M_\infty = 7.99, \quad Re_{r_n} = \rho_\infty^* U_\infty^* r_n^* / \mu_\infty^* = 33\,449$$

$$p_t^* = 4 \times 10^6 \text{ Pa}, \quad T_t^* = 750 \text{ K}$$

$$\gamma = 1.4, \quad Pr = 0.72, \quad \text{Gas constant} = 286.94 \text{ Nm kg}^{-1} \text{ K}^{-1}$$

$$\text{Free-stream unit Reynolds number: } Re_\infty^* = 8.78 \times 10^6 \text{ m}^{-1}$$

$$\text{Blunt cone half-angle: } \theta = 7^\circ, \quad \text{zero flow angle of attack}$$

$$\text{Spherical nose radius: } r_n^* = 3.81 \times 10^{-3} \text{ m}$$

$$\text{Parameters in Sutherland’s viscosity law: } T_r^* = 288 \text{ K}, \quad T_s^* = 110.33 \text{ K}$$

$$\mu_r^* = 0.17894 \times 10^{-4} \text{ kg ms}^{-1}$$

where p_t^* and T_t^* are total pressure and total temperature, respectively. The body surface is a no-slip and adiabatic wall for the steady base flow solution. The total length

of the cone of the experimental model is $l^* = 1.016$ m. The corresponding Reynolds number at this length is $Re_l = 8.92 \times 10^6$.

The cone surface consists of two distinct sections: a spherical nose region followed by a straight conical section of 7° half-angle. The junction of the two sections of the cone surface is continuous up to the first surface derivatives. However, there is a finite jump in surface curvatures at the junction. This discontinuity in surface curvatures at the junction creates slight adverse pressure gradients along the cone surface after the junction.

As stated earlier in this paper, the origin of the Cartesian coordinate system, (x, y, z) , is located at the centre of the nose spherical cone, where the x -coordinate points from left to the right along the the centreline of the axisymmetric cone. In addition to x , a natural coordinate s is also used in this paper to measure the dimensionless curve length of a surface location started from the stagnation point. The non-dimensional s and x , which are normalized by the nose radius r_n^* , are related to each other by the following relation:

$$x = \begin{cases} -\cos(s) & (s \leq \frac{1}{2}\pi - \theta), \\ (s - \frac{1}{2}\pi + \theta) \cos \theta - \sin \theta & (s > \frac{1}{2}\pi - \theta), \end{cases} \quad (2)$$

where θ is the half-angle of the cone. In the current test case, $\theta = 7^\circ$.

In the experiments of Stetson *et al.*, the wall surface was close to, but not exactly, adiabatic. The actual surface temperatures were about 10% to 20% lower than those of an adiabatic wall in the same free stream. The stability and receptivity properties of hypersonic boundary layers are strongly affected by the changes in surface temperature. In this paper, only the case of an adiabatic wall for the steady base flow is considered. The case of an adiabatic wall is chosen because all previous LST studies (Malik *et al.* 1990; Herbert & Esfahanian 1993; Kufner *et al.* 1993) and Kufner & Dallmann (1994) on the same flow were based on the assumption of the adiabatic wall, with the exception of Kufner *et al.* (1993) and Kufner & Dallmann (1994) who studied the effects of wall temperatures in addition to the case of the adiabatic wall. Therefore, the same adiabatic wall is used in this study so that current results can be compared with those of the previous LST studies. The effects of wall temperature and other parametric effects require a separate study.

4. Free-stream forcing waves

In order to reproduce similar flow conditions to those used in Stetson *et al.*'s experiments, it is natural to introduce initial forcing waves to excite the instability waves in the boundary layer to study the receptivity process. In Stetson *et al.*'s experiments, the free stream is dominated by acoustic waves generated by the boundary layer over the wind-tunnel wall. Therefore, we simulate the stability experiment by imposing free-stream acoustic disturbances. Since the wave fields in the experiments contain a wide range of second-mode frequencies, we simultaneously introduce two-dimensional planar fast acoustic waves with 15 independent frequencies, including dominant frequencies of second mode waves.

The wave fields are represented by the perturbations of instantaneous flow variables with respect to the local steady base flow variables. The free-stream perturbations of an arbitrary flow variable can be written in the following form:

$$q_\infty(x, y, t)' = |q'| \sum_{n=1}^{15} A_n \exp \left(i \left[n\omega_1 \left(\frac{x}{c_\infty} - t \right) + \phi_n \right] \right), \quad (3)$$

where c_∞ is the phase velocity in the free stream, and q represents any of the flow variables, including velocity components, density, pressure and temperature. In the equations above, $|q'|A_n$ is the free-stream wave amplitude of a given flow variable q at the n th frequency of

$$\omega_n = n\omega_1 \quad (n = 1, 2, \dots, 15), \quad (4)$$

where ω_1 is the minimum frequency of the wave packet. The minimum frequency ω_1 is chosen such that the frequencies span the dominant second-mode frequencies observed in the experiment. The relative amplitude A_n of a given wave frequency ω_n is determined according to figure 17 of Stetson & Kimmel (1992), such that,

$$\sum_{n=1}^{15} A_n^2 = 1. \quad (5)$$

Since the wave components of different frequencies are linearly independent, the initial phase angles, ϕ_n , of the forcing acoustic wave at frequency ω_n are chosen randomly. The forcing frequencies can also be represented by a dimensionless frequency F_n defined by

$$F_n = 10^6 \frac{\omega_n^* v^*}{U_\infty^{*2}}. \quad (6)$$

For fast acoustic waves in the free stream, perturbation amplitudes of non-dimensional flow variables satisfy the following dispersion relations:

$$|\rho'|_\infty = |p'|_\infty / \gamma = |u'|_\infty M_\infty = \epsilon M_\infty, \quad (7)$$

$$|s'|_\infty = |v'|_\infty = 0, \quad (8)$$

where ϵ is a dimensionless number representing the total amplitude of the group of 15 free-stream fast acoustic waves. In this paper, only linear receptivity is considered by using a very small value of ϵ .

The numerical simulation for an unsteady hypersonic boundary-layer receptivity problem is carried out in three steps. First, a steady base flow field is computed by advancing the unsteady flow calculations to convergence with no disturbances imposed in the free stream. Secondly, unsteady viscous flows are computed by imposing free-stream perturbations given by (3) to the steady base flow solution. The unsteady simulation is carried out for 20 to 50 time periods until the unsteady flow reaches a temporal periodic state. Thirdly, the unsteady computations are carried out for a number of additional periods in time to record the perturbations. A temporal Fourier transform is performed on the perturbation variables to obtain the Fourier amplitudes and phase angles of the perturbations of the unsteady flow variables for each individual frequency throughout the flow field.

5. Steady base flow solution

The steady base flow solution is obtained first by computing the flow to a steady state without free-stream forcing waves. The simulation is carried out by adopting a multi-zone approach using 35 zones with a total of 4700×121 grid points for the axisymmetric flow field from the nose to the 280 nose radius surface station downstream.

For their LST calculations, Esfahanian (1991) and Herbert & Esfahanian (1993) performed highly accurate steady base flow calculations of the same flow as considered

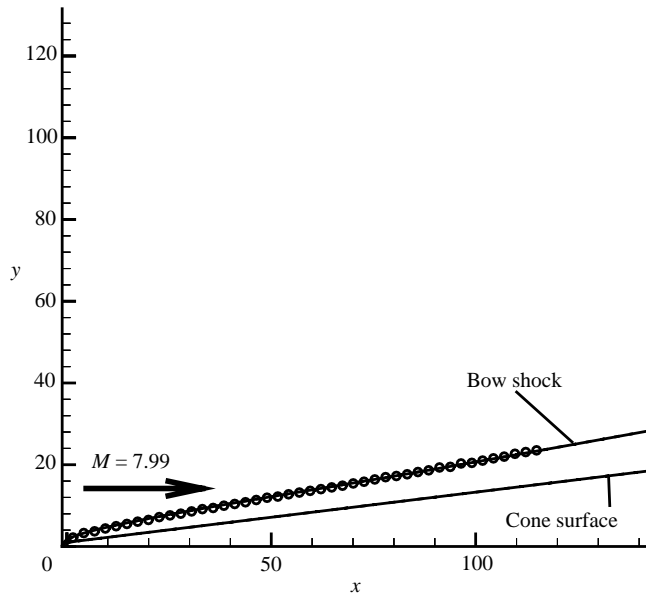


FIGURE 1. \circ , The experimental bow shock shape of Stetson *et al.* (1984) is compared with —, the current numerical solution.

in this paper. The thin-layer approximation of the Navier–Stokes equations was used in their computations with a set of 1300×100 grid points. Though lower than the grid resolution used in the current study, Esfahanian & Herbert’s mean-flow calculations had the highest grid resolution among all previous published calculations on this flow field. In this paper, the steady base solution of the full Navier–Stokes equations is compared with that of Esfahanian (1991) and Herbert & Esfahanian (1993) and the experimental results of Stetson *et al.*

Figure 1 compares the shape of the bow shock measured by Stetson’s experiment and computed by the current simulation. In the simulation, the bow shock shape, which is not known in advance, is obtained as the solution for the outer computational boundary. The experimental shape of the bow shock measured by Stetson *et al.* is marked by symbols in the same figure. The figure shows that the numerically computed bow shock agrees very well with the experimental measurements. The shape of the bow shock obtained by Esfahanian & Herbert’s calculations has also been compared with the current solution. Though the comparison is not presented here owing to the length limitation, it is found that the numerical shock shape obtained by Esfahanian & Herbert agrees very well with the current results as well as experimental results. Therefore, the bow-shock shape is accurately predicted by the high-order shock-fitting scheme used in the current computations.

Figure 2 compares three sets of steady pressure and temperature distributions along the cone surface. It shows that the surface pressure predicted by the current calculations can match both experimental results and Esfahanian & Herbert’s numerical results. The maximum wall pressure is reached at the stagnation point. The surface pressure drops sharply as flow expands around the nose region. Because of the discontinuity in surface curvatures at the junction of the spherical nose and straight cone, the flow experiences an overexpansion at the junction and goes through a recompression along the cone surface afterward. As a result, there is slight adverse

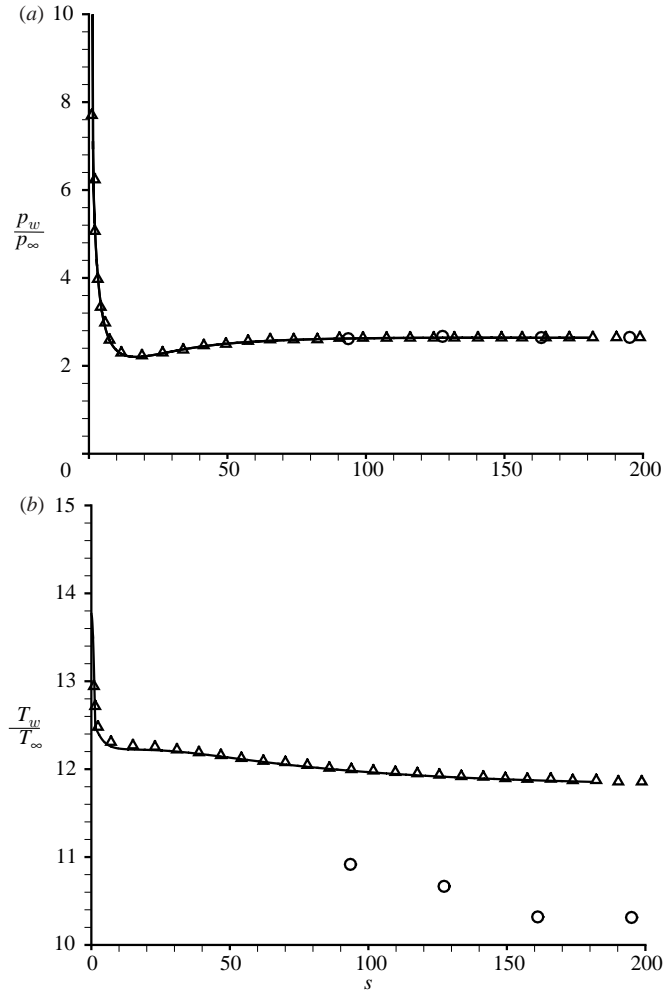


FIGURE 2. (a) Steady pressure and (b) temperature distributions along the cone surface. \circ , The experimental results of Stetson *et al.* (1984) and \triangle , numerical results of Herbert & Esfahanian (1993) are compared with —, the current results.

pressure gradient along the surface locations after the junction. Further downstream, the surface pressure approaches a constant value. As for the comparison of the steady surface temperature distributions, this figure shows that the current results agree very well with the results of Herbert & Esfahanian. The maximum steady adiabatic wall temperature is also reached at the stagnation point. The steady adiabatic wall temperature drops as x increases along the surface. However, both sets of independently obtained numerical solutions with an adiabatic wall predict higher surface temperatures than the experimental results, which indicates that the cone surface in Stetson *et al.*'s experiments was not perfectly adiabatic. The experimental surface temperatures are about 10% to 20% lower than those of the numerical solutions for an adiabatic wall.

The tangential velocity profiles across the boundary layer at a surface location of $s = 94$ and 128 are compared in figure 3. The experimental measurements could only reach a certain minimum distance away from the wall surface because of the size limit

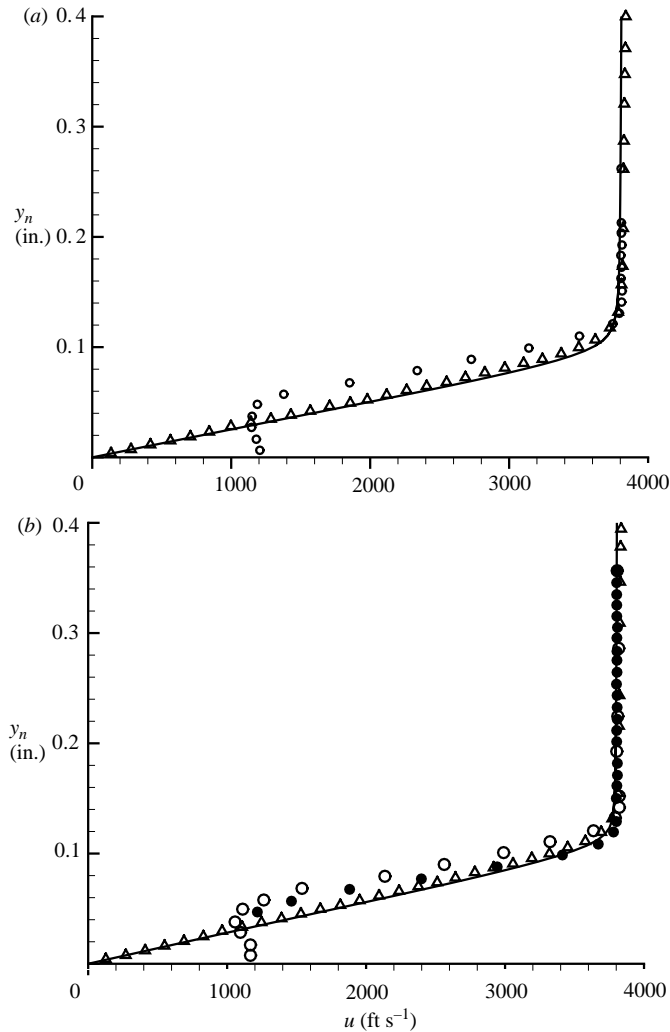


FIGURE 3. Tangential velocity profiles along the wall-normal direction at the surface locations of (a) 94 nose radii and (b) 128 nose radii. The experimental results are obtained by Stetson *et al.* (1984): (a) ○, run 105; (b) ●, run 76; ○, run 104. —, current results; △, Herbert & Esfahanian (1993).

of the experimental probes. The figures show that the current numerical results agree very well with those obtained by Herbert & Esfahanian's (1993) calculations. The computed velocity magnitudes agree well with the experimental measurements in the flow region outside the boundary layer. The computed velocities inside the boundary layer, however, are slightly larger than the corresponding experimental values. The cause of the discrepancy between the two sets of independently obtained numerical simulation and the experimental results is currently not known. It is possible that the discrepancy is a result of the uncertainty in experimental measurements. In addition to the velocity profiles shown in figure 3, the agreements between the two sets of numerical solutions in all other variables are also very good. The profiles of current pressure and temperature at the $s = 54$ surface station are compared with those of Esfahanian & Herbert in figure 4. No experimental results are available for

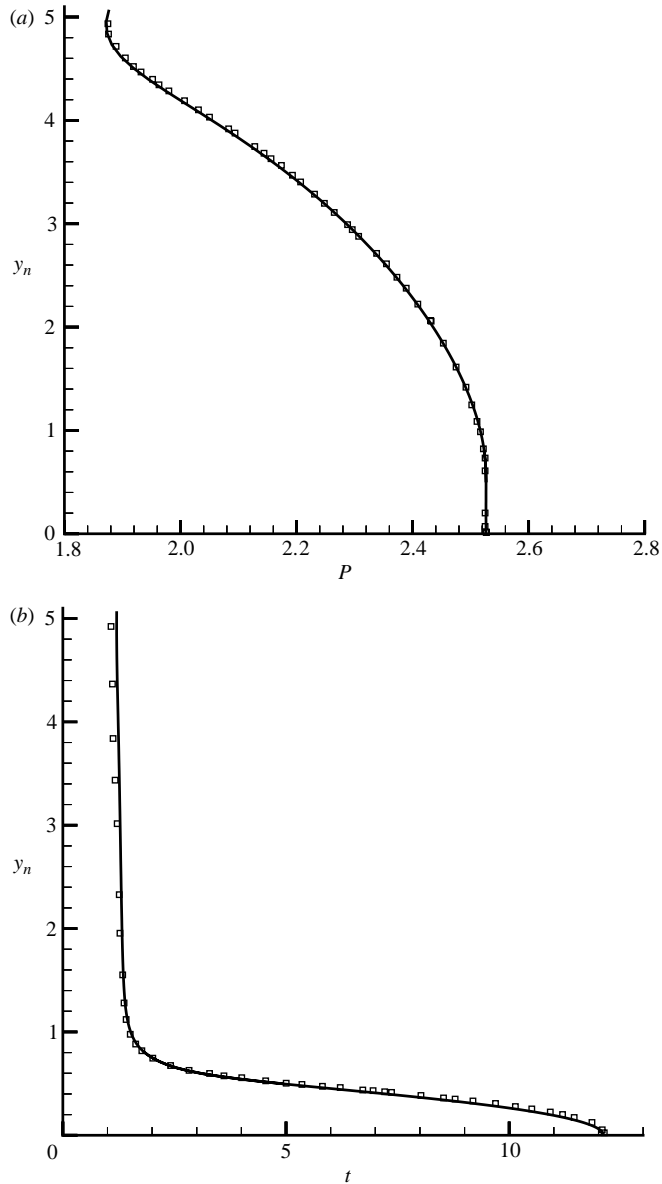
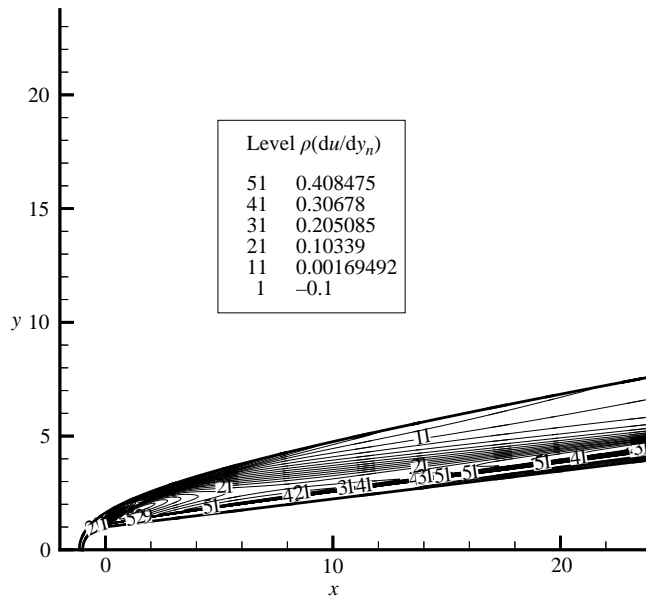


FIGURE 4. (a) Pressure and (b) temperature profiles at the surface station of $s = 54$. —, Current results are compared with \square , those of Esfahanian (1991).

comparison in these figures. Again, current results agree very well with the solution by Esfahanian & Herbert. Figure 4 shows that, while the pressure is not constant in the wall normal direction, it is close to constant across the boundary layer in the near-wall region. On the other hand, the temperature profile shown in figure 4 is a typical temperature profile across an adiabatic-wall compressible boundary layer.

The effects of entropy layer on steady base flow are examined by comparing the steady flow solution at different surface stations along the cone surface. The entropy layer can be characterized by several parameters. In this paper, we study the effects of the entropy layer by means of a parameter, $\rho(du_t/dy_n)$, the peaks of which are

FIGURE 5. Contours of $\rho(du_t/dy_n)$.

generalized inflection points (GIPs). Lees & Lin (1946) showed that the existence of a GIP is a necessary condition for the inviscid instability in a compressible boundary layer. Figure 5 shows the contours of $\rho(du_t/dy_n)$ obtained by the current simulation. Only a small part of the flow field near the nose region is shown in the figure in order to demonstrate the entropy layer more clearly. The figure shows that there is a peak in the contour lines outside the boundary layer. This peak is located initially behind the bow shock and outside the boundary layer. The peak gradually approaches the wall and merges with the boundary layer on the wall. This is a clear indication of the creation of the entropy layer at the bow shock and the subsequent effects of the entropy layer on the steady base flow field.

Figure 6 plots the $\rho(du_t/dy_n)$ profiles at four surface locations ranging from $s = 7.87$ near the nose to $s = 46.96$ downstream. Again, in the region near the nose, there is an entropy layer outside the boundary layer. This entropy layer is represented in a peak located initially behind the bow shock and outside the boundary layer. In the region near the nose of $s = 7.87$ and $s = 19.75$, figure 6 shows two distinct regions in the $\rho(dy_n/du_t)$ profiles with two separate peaks: one inside the boundary layer and another outside the boundary layer. The latter peak is created by the entropy layer. Since the generalized inflection point is located at $d(\rho(du_t/dy_n))/dy = 0$, the additional peak outside the boundary layer can be responsible for the inviscid instability in the entropy layer. At the location of $s = 7.87$, the peak associated with the entropy layer is located approximately at $y_n = 1$. As the entropy layer moves downstream, this peak gradually moves towards the wall, and eventually merges with the boundary layer on the wall. As s increases to 32.87 in figure 6, the peak associated with the entropy layer is about to merge with the peak inside the boundary layer. Further downstream at $s = 46.96$, the peak outside the boundary layer has been absorbed, or swallowed, by the boundary layer. After that, there is only one peak in the profile. Eventually, further downstream the profiles become essentially similar to those of a sharp cone without the entropy-layer effects.

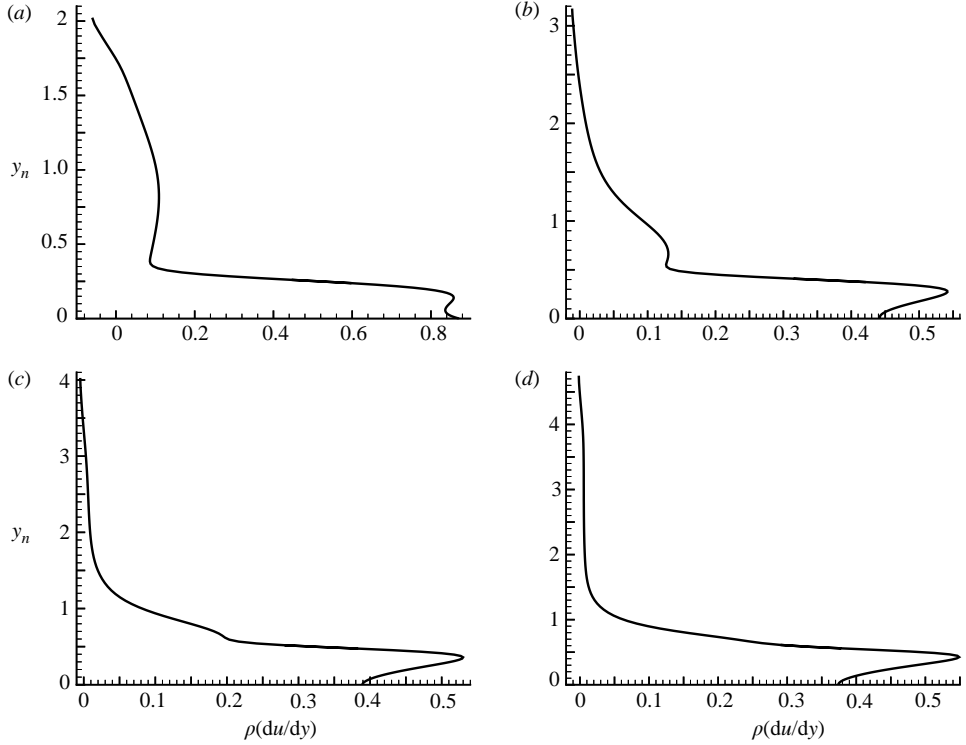


FIGURE 6. The profiles of $\rho(du_t/dy_n)$ along the wall-normal direction at four surface locations, (a) $s = 7.87$, (b) 19.75 , (c) 32.87 , (d) 46.96 .

6. Linear stability theory (LST)

6.1. Growth rate comparisons

In this paper, the LST is used to identify the main components of boundary-layer disturbances from the results of numerical simulations. In the LST, a local Reynolds number, R , based on the length scale of the boundary-layer thickness is used:

$$R = \frac{\rho_\infty^* u_\infty^* L^*}{\mu_\infty^*}, \quad (9)$$

where L^* is the length scale of the boundary-layer thickness defined as

$$L^* = \sqrt{\frac{\mu_\infty^* s^*}{\rho_\infty^* u_\infty^*}}, \quad (10)$$

where s^* is the natural surface coordinate defined as the curve length along the wall surface measuring from the nose. The relation between R and local Reynolds number Re_s based on s^* is

$$R = \sqrt{Re_s} = \sqrt{s Re_{r_n}}. \quad (11)$$

A non-dimensional angular frequency ω and wavenumber α are normalized by u_∞ and L^* :

$$\alpha = \alpha^* L^*, \quad (12)$$

$$\omega = \omega^* L^* / u_\infty^*. \quad (13)$$

The dimensionless frequency F is related to ω by

$$\omega = 10^{-6}FR. \quad (14)$$

The LST is based on the normal mode analysis under a local parallel-flow assumption. Specifically, the linear fluctuations of flow variables are decomposed into the following normal mode form:

$$q' = \hat{q}(y_n) \exp(i(-\omega t + \alpha s)), \quad (15)$$

where $\hat{q}(y_n)$ is the complex amplitude of the disturbances, n and s are the local natural coordinates along the wall-normal and surface directions respectively, $\alpha = \alpha_r + i\alpha_i$, is the streamwise complex wavenumber. The variable q stands for any of the independent flow variables u , v , w , p , ρ (or T). In a spatial linear stability analysis, for a given frequency ω , complex parameter α and complex function $\hat{q}(y)$ are obtained as an eigenvalue and eigenfunction of the stability equations. For a spatial stability problem, ω is a real number while α is a complex wavenumber. The real and imaginary parts of α , α_r and α_i , represent the spatial wavenumber and growth rate of a wave mode, respectively. A linear wave mode is unstable when α_i is negative. The real part of the wavenumber α_r is related to the phase velocity of a wave mode by

$$a = \frac{\omega}{\alpha_r} = \frac{10^{-6}FR}{\alpha_r}, \quad (16)$$

where a is the non-dimensional phase velocity normalized by the free-stream velocity.

In the current study, an axisymmetric LST computer code based on the multi-domain spectral method of Malik (1990) is developed for analysing the linear stability properties of axisymmetric compressible boundary layers. The asymptotic boundary condition (Malik 1990) is used near the shock boundary in the LST. The shock effects are not considered in the LST because most comparisons between the LST and the DNS in this paper are located downstream with $x > 100$. The shock effects on the LST results will be proved to be negligible far away from the leading edge ($x > 100$) through the comparison with the DNS results. Before being used to carry out the linear stability computations to identify instability modes in the hypersonic boundary layer, the LST code is validated by comparisons with other published LST results and experimental results. The grid independence of the LST results is also verified by comparing results of different grid resolutions. Two sets of grids contain 100 and 200 grid points across the boundary layer, respectively. It is found that the results from two sets of grids are almost identical to each other. Based on this assessment, the grid resolution of 100 grid points is used in the LST calculations in the current study.

Figure 7 compares spatial growth rates at the surface station of $s = 175$. The experimental results of Stetson *et al.*, and other published LST results (Malik *et al.* 1990; Herbert & Esfahanian 1993), are plotted in the same figure for comparison. The figure shows that the current LST results on the second-mode growth rates ($100 \text{ kHz} < f^* < 170 \text{ kHz}$) compare well with the other LST results. The differences between the current LST results and those of other authors are mainly caused by different steady base flow solutions used in different LST computations. The current second-mode growth rates are closer to those of Esfahanian & Herbert than those of Malik *et al.* A possible reason for such a close agreement is that the grid resolutions of these two calculations of the steady base flow solutions are relatively higher. In this figure, the growth rates of the first mode in the current calculations are for two-dimensional disturbances only, while those of Malik *et al.* are the most unstable oblique first mode. As a result, the two sets of results do not agree in the first mode

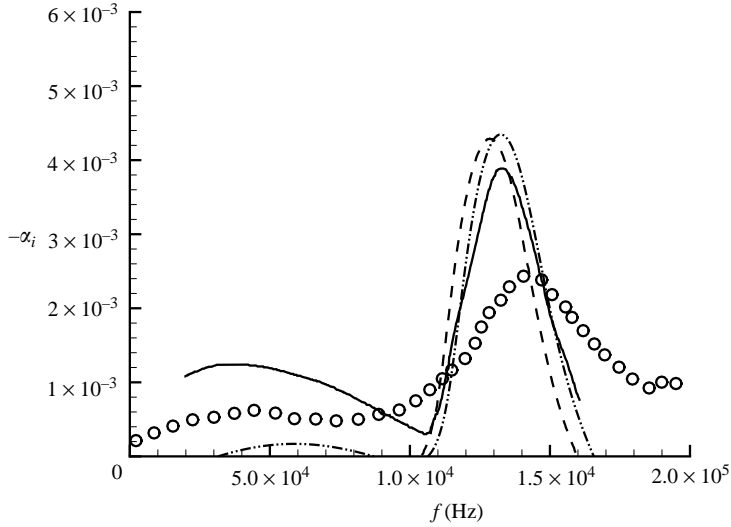


FIGURE 7. Comparison of the growth rates of the Mack modes predicted by LST —, Malik *et al.* (1990); ---, Herbert & Esfahanian (1993); -·-, current results and measured by \circ , the experiments of Stetson *et al.* (1984) at $s = 175$ ($x = 172$).

region of lower frequencies. Since only two-dimensional receptivity is considered in this paper, no effort is made to obtain the growth rates of the most unstable three-dimensional oblique first Mack mode in the current LST calculations.

As discussed earlier in this paper, figure 7 shows that the LST predicts much higher second-mode growth rates than the experiments did. The disagreement between experimental growth rates and the LST results shown in figure 7 may be due to nonlinear effects in the experimental waves or other reasons. Since the numerical simulation of the current paper involves minimum simplifications in flow models, the growth rates predicted by the full Navier–Stokes simulation are expected to shed light on the reason for the difference in growth rates predicted by LST and those observed in experiments. Figure 7 also shows that at the surface location of 175 nose radii, the second mode instability range is between 100 kHz and 170 kHz. The first mode unstable frequency range is lower than 100 kHz. In other words, second mode waves of frequencies between 100 kHz and 170 kHz, and first mode waves at lower frequencies should become unstable at the surface station of 175 nose radii.

In order to compare the growth rates of the second Mack mode computed by LST and those simulated by the current direct numerical simulation, we also conducted a separated simulation where the forcing disturbances are introduced by surface blow-and-suction. The forcing waves contain the same set of 15 frequencies. Figure 8 compares wavenumbers and the growth rates of the second mode between the LST results and simulation results at $n = 8$ ($f^* = 119.4$ kHz). The figure shows a perfect agreement between the wavenumbers, and a close agreement between the growth rates. This comparison shows that the LST is an accurate tool in computing hypersonic boundary-layer instability. On the other hand, the disagreements in the early region near the blow-and-suction slot ($x < 200$) are caused by the transient effects from the blowing and suction.

Besides the growth rate comparison, the second-mode eigenfunctions of the current LST calculations are compared with Esfahanian (1991) LST results. Figure 9 compares the second mode temperature perturbation eigenfunctions obtained by the current

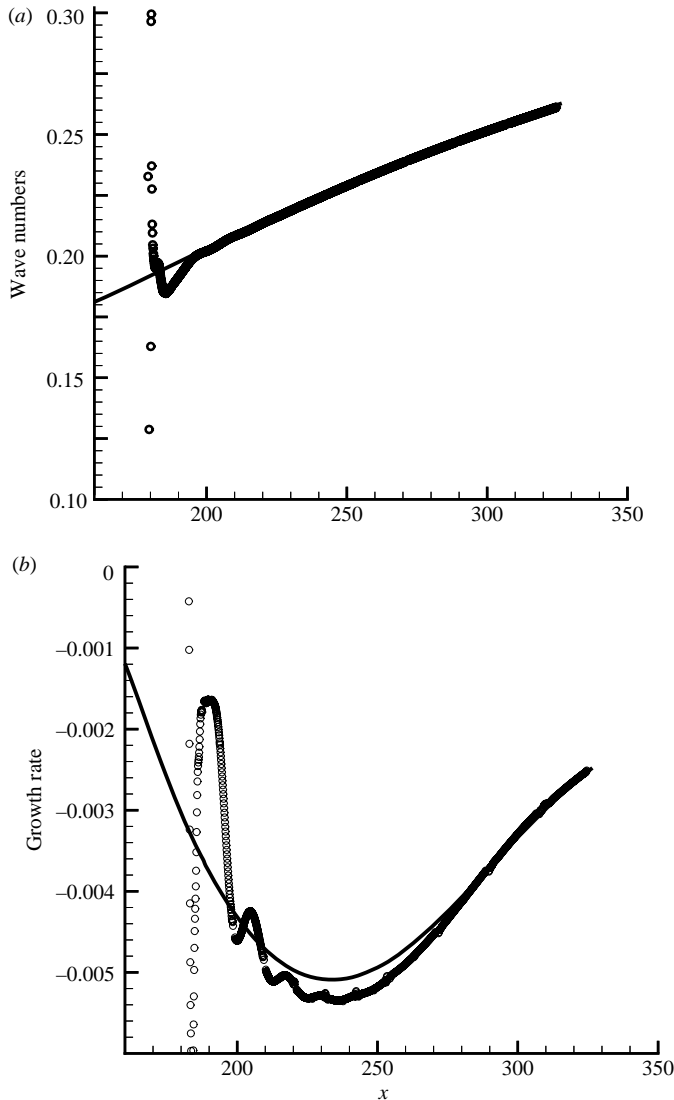


FIGURE 8. Comparison of (a) wavenumbers and (b) growth rates obtained by —, LST prediction of the second mode and \circ , numerical simulation of the full Navier–Stokes equations ($n = 8$, $f^* = 119.4$ kHz). The disturbances in the simulation are induced by surface blow-and-suction.

LST computations and those of Esfahanian & Herbert for $s = 175$ and $\omega = 0.1934$ (127.56 kHz). There is excellent agreement between the two independently obtained LST results for the profiles of the second-mode temperature perturbations across the boundary layer. Though not shown here, good agreements are also observed in comparisons of eigenfunctions for all other flow variables between the current LST results and those of Esfahanian & Herbert.

6.2. Linear stability analysis of wave modes

The previous LST studies on Stetson's blunt cone (Malik *et al.* 1990; Herbert & Esfahanian 1993; Kufner *et al.* 1993; Kufner & Dallmann 1994) mainly focused on the calculations of the growth rates of the unstable first and second Mack modes.

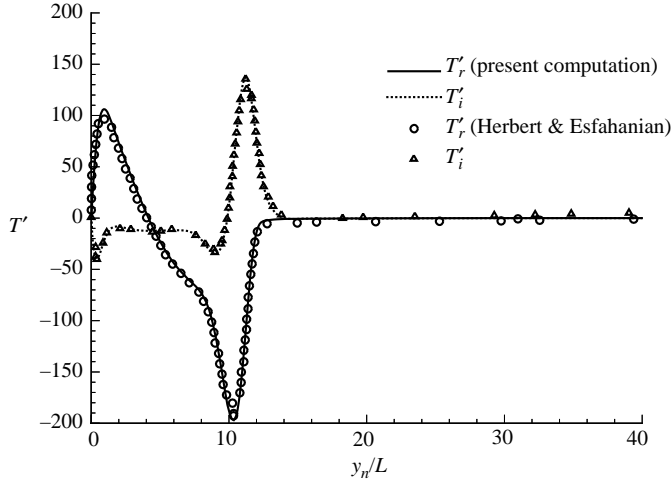


FIGURE 9. Comparison of the second mode eigenfunctions of T' between the current LST results and those of Herbert & Esfahanian (1993) ($s = 175$, $\omega = 0.1934$, $f^* = 127.56$ kHz).

Other boundary-layer wave modes, which are always stable, have not been studied. In our previous receptivity study (Ma & Zhong 2002, 2003a, b), it was found that a family of other wave modes, which are always stable in a linear stability analysis, play an important role in the receptivity process. They were termed modes I, II, III, etc. by Ma & Zhong. In order to understand the receptivity process, it is necessary to compute the characteristics of these stable wave modes in the current axisymmetric flow in addition to the traditional unstable Mack modes. So far, the characteristics of these stable wave modes in hypersonic flows with nose bluntness have not been studied. Therefore, an LST study is carried out for the current case.

Figure 10 shows the spectra of eigenvalues, α , at $\omega = 0.1934$, $s = 175$. The relative positions of mode I and the second Mack mode in the spectra are marked by circles. When ω increases gradually, the relative positions of mode I and the second mode will gradually change accordingly. We can track the position of each mode and obtain its trajectory. The solid line and dashed line in figure 10 represent the trajectories of mode I and the Mack modes with increasing ω , respectively. It shows that mode I starts from the left-hand acoustic spectrum branch (Mack 1984, 1987) for very low frequency ($\omega < 0.01$), and passes across the entropy/vorticity spectrum branch in the middle with increasing ω . On the other hand, the trajectories of the second mode start from the right-hand acoustic spectrum branch and approach the entropy/vorticity spectrum branch in the middle with increasing ω . The trajectory of mode II is very similar to that of mode I, but the starting frequency is much higher. Here, modes I and II are in fact ‘multiple-viscous solutions’ by Mack (1987) and by Eibler & Bestek (1996).

Figure 11 shows the distributions of the phase velocities (equation (16)) of three discrete modes, mode I, mode II and the Mack modes (including the first and the second modes), as functions of frequencies at $s = 175$. The phase velocities of the fast acoustic wave ($1 + 1/M_\infty$), entropy/vorticity wave (1), and slow acoustic wave ($1 - 1/M_\infty$) are also shown in the figure for comparison. Both mode I and mode II originate from the fast acoustic wave with an initial phase velocity of $1 + 1/M_\infty$. Before these two modes become distinct modes, their eigenvalues merge with the fast acoustic spectrum branch. After these two wave modes appear as discrete modes, their phase velocities decrease gradually with increasing ω . As a result, the phase-velocity

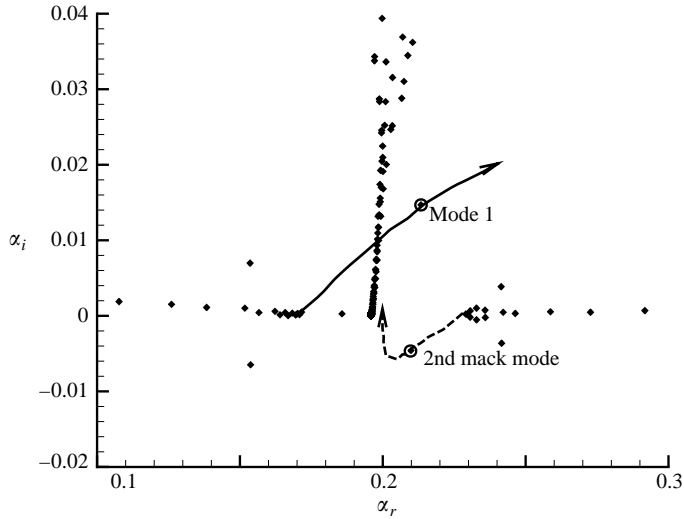


FIGURE 10. Spectra of eigenvalues at a fixed frequency of $\omega = 0.1934$ ($f^* = 127.56$ kHz), at the surface station of $s = 175$ ($x = 172$). The relative positions of mode I and the second Mack mode in the spectra are marked by circles. The solid line and dashed line show the trajectory of changes of mode I and the second mode, respectively, when ω increases.

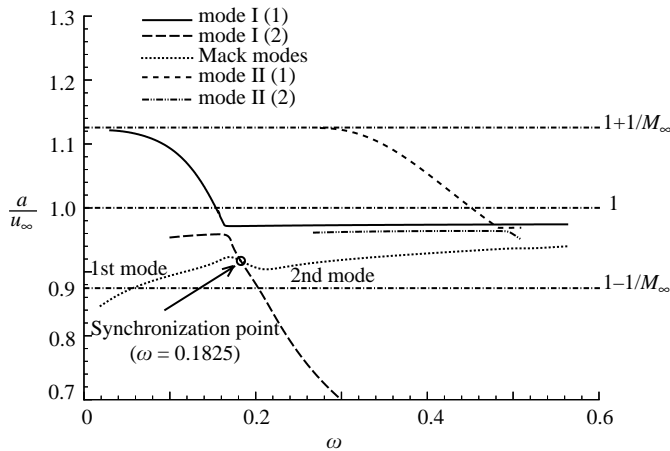


FIGURE 11. Distributions of the phase velocities of three discrete modes, mode I, mode II and the Mack modes (including the first and second modes), as functions of frequencies at the surface station of $s = 175$.

differences between mode I (or mode II) and the fast acoustic waves become larger as ω increases. On the other hand, the first mode originates from the slow acoustic wave side with an initial phase velocity close to $1 - 1/M_\infty$. Furthermore, the phase velocity curve of the first mode shows an opposite trend when ω increases. As ω increases, the phase velocity of the first mode increases and intersects with the phase velocity curve of mode I at the location with $\omega = 0.1825$. After passing the intersection point, the first mode convert to the second mode. As was shown in our previous study (Ma & Zhong 2003a), the first mode and the second mode identified by Mack are in fact different sections of a single wave mode, which is confirmed in the phase

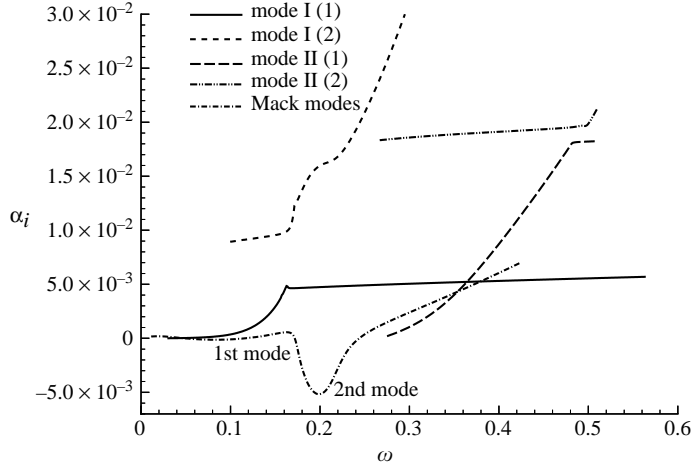


FIGURE 12. Distributions of the growth rates of three discrete modes, mode I, mode II and the Mack modes (including the first and the second modes), as functions of frequencies at the surface station of $s = 175$.

velocity curve shown in figure 11 and growth rate curve shown in figure 12. Therefore, both the first and the second Mack modes are simply called Mack modes in order to be consistent with Mack's generally accepted terminology. In the vicinity of the intersection point between mode I and the first mode, the phase velocity of the first mode drops a little, and phase velocity of the Mack modes increases again after it clearly becomes the second mode. Similarly, Mode II eventually intersects with the Mack mode at a high frequency.

Figure 11 also shows that the distributions of phase velocities for both mode I and mode II are discontinuous. In fact, mode I (or mode II) merges with the middle entropy/vorticity spectrum branch when their trajectories pass across it (figure 10). Later, another eigenvalue from this spectrum branch becomes discrete mode I. As a result, there is a gap in the phase velocity curves of mode I (or mode II) shown in figure 11. Consequently, there are two branches of mode I (or mode II) in the phase velocity curves. They are labeled as mode I(1) and mode I(2) for mode I, mode II(1) and mode II(2) for mode II in the figure, respectively. With the further increase of ω , the phase velocities of mode I (or mode II) continue to decrease further and eventually intersect with the phase velocity curve of the Mack modes.

It should be noted that similar results were also observed in our previous study for hypersonic flow over a wedge (Ma & Zhong 2003c). In Ma & Zhong (2003c), the characteristics of mode I(1) and mode I(2) were investigated by using both DNS and LST. Mode I(1) and mode I(2) are indeed two different eigenvalues from the LST results. However, near the jump region, the profiles of mode I(1) and mode I(2) are very close to each other. In the DNS study, there is continuous development of mode I waves when mode I(1) was introduced from the inlet in upstream. In other words, the jump in the phase speed curve for mode I from the LST results is not shown in the DNS results. Moreover, the phase speed curve from the DNS can match that of mode I(1) and mode I(2). Therefore, it is reasonable to conclude that mode I(1) and mode I(2) are the same physical mode, so are mode II(1) and mode II(2).

In the receptivity study, we are more interested in the resonant interaction between mode I and the first mode. At the intersection point between mode I and the first mode ($\omega = 0.1825$ for $s = 175$), mode I is synchronized with the Mack mode because the two

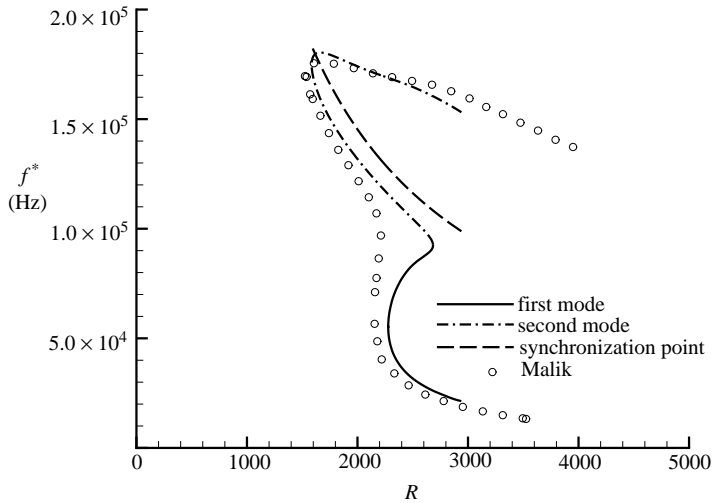


FIGURE 13. Comparison of the current neutral stability curve of the Mack modes with Malik's (1990) results. The synchronization locations between mode I and the Mack modes are also marked in the figure.

modes have the same frequency, phase velocity and wavenumber. Therefore, there is a resonant interaction between mode I and the Mack mode near this intersection location. In addition, both modes have very similar profiles of perturbation eigenfunctions across the boundary layer at this location. The only exception is that the two modes have different growth rates (α_i). In fact, the growth rates of the Mack modes have already been shown in figure 7 at $s = 175$ for a range of frequencies. Here, the growth rates of the Mack modes at the same station are compared with those of other boundary-layer normal modes in figure 12. While the growth rates of the Mack modes are continuous, there are gaps in the growth rate curves for mode I and mode II. The figure shows that both mode I and mode II are always stable. When they initially appear at relatively low frequency, these two modes are close to neutrally stable with zero growth rates. As ω increases, their growth rates are always on the stable side and rapidly become more stable. On the other hand, the Mack modes are unstable in multiple regions of different frequencies. The Mack modes are slightly unstable in the range of ω between 0.0485 and 0.126 ($33.1 \text{ kHz} < f^* < 86.1 \text{ kHz}$). The Mack mode in this range is the conventional first mode identified by Mack (1984). In the range of ω between 0.171 and 0.243 ($116.7 \text{ kHz} < f^* < 165.9 \text{ kHz}$), the unstable Mack modes are the conventional second mode identified by Mack. In this range, the growth rates of the second mode increase to a peak and decay afterward. The second Mack mode has the largest growth rate at $\omega = 0.198$ ($f^* = 135 \text{ kHz}$), $s = 175$.

Another important characteristic of boundary-layer instability modes is the neutral stability curve for frequencies versus Reynolds numbers. The current results on neutral stability curves are compared with that of Malik (1990) in figure 13. Dimensional frequencies f^* are used in the figure because the experimental results were presented using dimensional frequencies. The dimensional frequencies can be converted easily to dimensionless frequencies F by using (6). The synchronization locations between mode I and the Mack modes are also plotted in the same figure because the synchronization locations between mode I and the Mack modes play an important role in the receptivity process (Ma & Zhong 2002, 2003a, b). There are two peaks in the neutral

stability curve. The first peak with lower frequencies (lower than 100 kHz) is for the first Mack mode instability, while the second peak with higher frequencies (higher than 100 kHz) is for the second mode instability.

Overall, there is good agreement between the present result and Malik's result in the neutral stability curve, (13). There are some slight differences between the two sets of results, especially in the border region between the first and second Mack modes, owing to different steady base flow solutions used in the two LST calculations. The current steady base flow solution is obtained with a much higher grid resolution than that used in Malik's LST calculations. Based on the current results, the critical local Reynolds number (R) for the onset of the boundary-layer instability is the second mode instability at the surface location of 1580, which corresponds to $s = 75$ and $x = 72.5$. This critical value is very close to Malik's result $R = 1540$ for $s = 70.9$ and $x = 68.8$. Below this critical Reynolds number, all boundary-layer wave modes are stable. The first unstable two-dimensional first modes appear at $R = 2270$, which corresponds to the $s = 154$ surface station. Figure 13 also shows that both the first and the second modes are stable when frequencies are higher than 180 kHz.

7. Receptivity to free-stream noise

Having obtained the steady base-flow solution by numerical simulations and the characteristics of the boundary-layer normal modes by the LST, the receptivity to free-stream fast acoustic waves is studied by numerical simulations. The free-stream forcing waves are a mixture of 15 independent planar fast acoustic waves of different frequencies, i.e.

$$f_n^* = n f_1^* \quad (n = 1, 2, \dots, N; N = 15), \quad (17)$$

where the lowest frequency is $f_1^* = 14.92$ kHz ($F_1 = 9.04$). The remaining 14 frequencies are multiples of f_1^* given by (17), where the highest frequency is $f_{15}^* = 223.8$ kHz ($F_{15} = 135.5$). The relative wave amplitudes among different frequencies in the free stream are set according to the experimental free-stream wave spectra reported by Stetson *et al.* The phase angles of the free-stream forcing waves of the 15 frequencies given by (3) are chosen randomly. The 15 sets of wave frequencies, relative amplitudes A_n , and phase angles used in the current receptivity simulation are given in table 1. The overall free-stream wave amplitude used in the simulation is $\epsilon = 6.2578 \times 10^{-4}$, which is sufficiently small that the receptivity process falls in the linear regime. Consequently, the wave components of 15 frequencies are independent, and they can be decomposed one from another by a temporal Fourier analysis. Since the receptivity results for a given frequency f_n are proportional to the values of A_n in a linear receptivity process, the particular value of A_n in forcing wave spectra used in a simulation are not critical.

The unsteady calculations are carried out until the solutions reach a periodic state in time. Temporal Fourier analysis is then carried out on the local perturbations of unsteady flow variables. A Fourier transform for the perturbation field of an arbitrary flow variable q leads to:

$$q'(x, y, t) = Re \left\{ \sum_{n=0}^N |q_n(x, y)| \exp[i(-n\omega_1 t + \phi_n(x, y))] \right\}, \quad (18)$$

where $n\omega_1$ is the frequency of the n th wave mode, $q'(x, y, t)$ represents an arbitrary perturbation variable. The Fourier transformed variables, $|q_n(x, y)|$ and $\phi_n(x, y)$, are spatially varying real variables representing the local perturbation amplitudes and phase angles at the wave frequency of $n\omega_1$. For perturbations on the body surface,

n	f_n^* (kHz)	F_n	A_n	ϕ_n (rad)
1	14.92	9.035	0.7692	2.4635(-6)
2	29.84	18.07	0.4162	0.1600
3	44.77	27.11	0.2827	2.2149
4	59.68	36.14	0.2065	4.1903
5	74.61	45.18	0.1707	6.0510
6	84.53	54.21	0.1406	5.2671
7	104.5	63.25	0.1132	2.1070
8	119.4	72.28	9.7164(-2)	5.7511
9	134.3	81.31	0.1081	5.0005
10	149.2	90.35	9.0781(-2)	5.2319
11	164.1	99.39	7.7722(-2)	2.1679
12	179.1	108.4	5.8428(-2)	5.4738
13	194.0	117.5	5.0729(-2)	0.5649
14	208.9	126.5	7.6987(-2)	5.5812
15	223.8	135.5	5.7108(-2)	4.4043

TABLE 1. Forcing acoustic wave components of 15 frequencies in the free stream.

we can compute local growth rate, α_i and local wavenumber α_r from the numerical perturbation fields by,

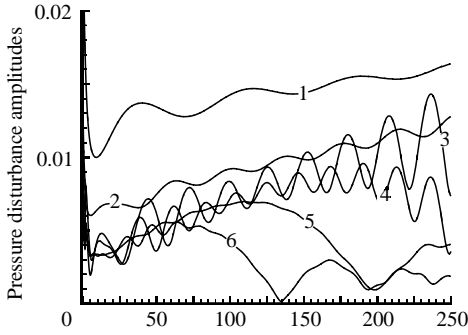
$$\alpha_i = -\frac{1}{|q_n|} \frac{d|q_n|}{ds}, \quad (19)$$

$$\alpha_r = \frac{d\phi_n}{ds}, \quad (20)$$

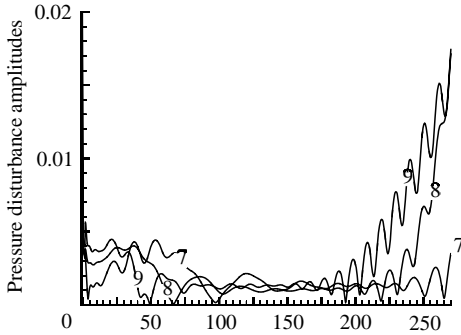
where $|q_n|$ can be any variables which disturbances do not make disappear at the wall surface, and the derivatives are taken along the natural coordinate s along the body surface. The wave modes induced in the boundary layer are identified by comparing the simulation results with the LST ones. If the flow perturbations of the simulation results in a local region of the boundary layer are dominated by a single wave mode, the parameters, α_r and α_i , computed by (19) and (20) are the wavenumbers and growth rates of this mode. In this case, α_i and α_r are smooth functions of x . On the other hand, if the simulation results contain simultaneously multiple wave modes in a local region of the boundary layer, α_i and α_r computed by (19) and (20) do not represent the wavenumbers and growth rates of a single wave mode. Instead, these two parameters represent a modulation of two or more wave modes. As a result, the distributions of α_i and α_r along the surface direction will be oscillatory functions of x . In this case, further decomposition of different wave components is required in order to obtain the growth rates and wavenumbers of the individual wave modes.

Although the steady base flow has an adiabatic wall with a zero temperature gradient on the wall, it has been generally accepted that the temperature perturbations should be set to zero because of the relatively high frequencies of the second mode. In the current study, both cases of different temperature perturbation conditions on the wall, i.e. $\partial T'/\partial y_n = 0$ and $T' = 0$, are simulated with the same adiabatic base flow. It is found that the overall stability and receptivity characteristics are similar for both cases; but, the case of adiabatic temperature perturbations has much stronger instability than the case of isothermal temperature perturbations. Only the results of the test case of $T' = 0$ boundary condition are presented in this paper because this case is closer to the actual instability of the second mode.

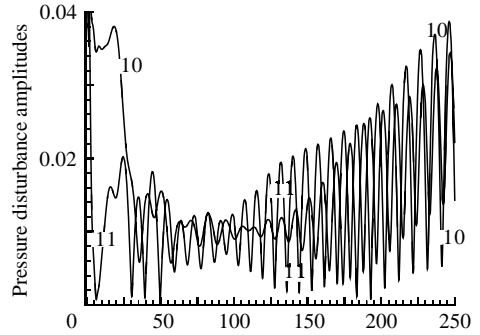
(a)



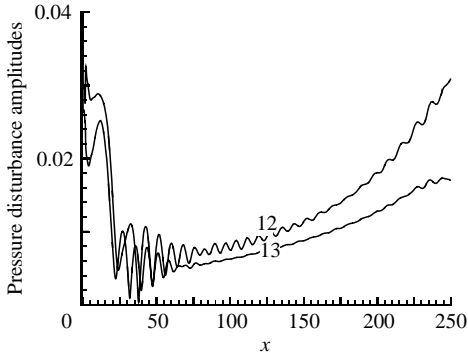
(b)



(c)



(d)



(e)

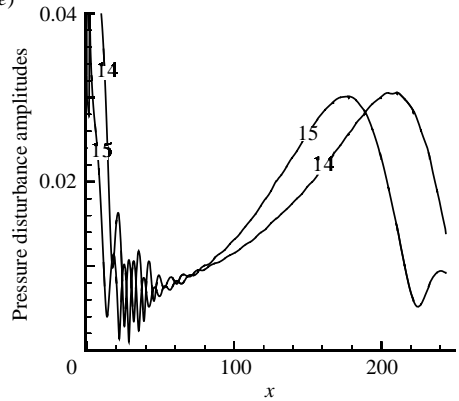


FIGURE 14. Amplitude distributions of the induced pressure perturbations along the cone surface. The lines represent 15 different frequencies of $f_n^* = n f_1^*$, where $f_1^* = 14.922$ kHz and $n = 1, 2, \dots, 15$.

7.1. General characteristics of the induced waves

Figures 14 shows the distributions of amplitudes of the pressure perturbations, $|p_n(x, y)|$, for the 15 forcing frequencies along the cone surface. The pressure perturbation amplitudes, $|p_n(x, y)|$, are obtained by a temporal FFT calculation according to (18). Each line in figure 14 represents one of the 15 frequencies given by (17). The

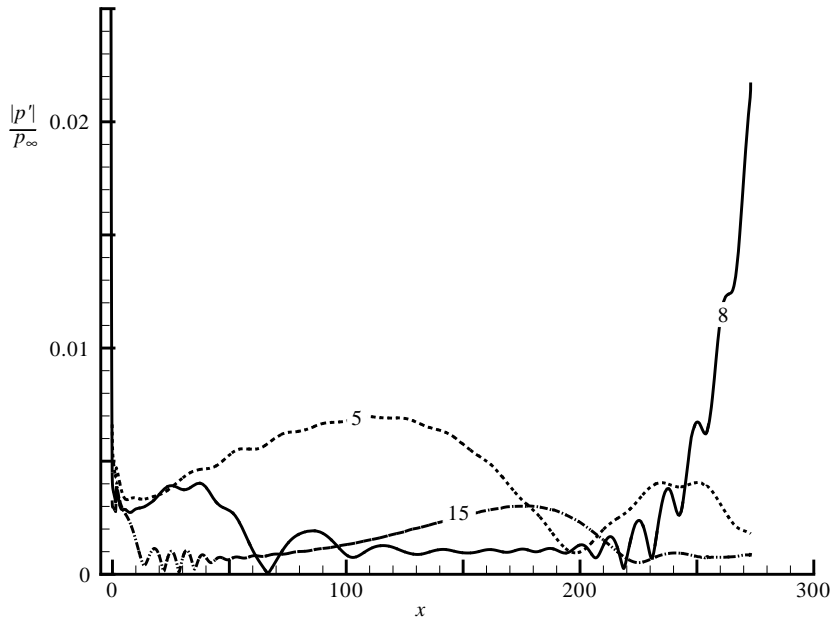


FIGURE 15. The evolution of the amplitudes of the pressure perturbations along the wall at three frequencies (for \dots , $n = 5$, $—$, 8 , $-\cdot-$, 15).

relative amplitudes in the free-stream forcing waves for each frequency are different because they are chosen to be proportional to those of Stetson *et al.*'s experiments, as shown in table 1. Figure 14 shows that the receptivity process leads to complex induced wave structures in the boundary layer. The wave structures are different for different frequencies. For perturbations of a fixed frequency, the disturbance wave structures are also different for different sections of the cone surface.

Figure 14(a) shows the amplitude development along the cone surface for the first group of the six lowest frequencies, ranging from 14.9 kHz to 84.5 kHz ($n = 1, \dots, 6$ in table 1). The figure shows that the amplitude distributions for four of the six frequencies ($n = 1, 2, 5, 6$) are relatively smooth, which is an indication that the perturbations are dominated by a single wave mode. On the other hand, the amplitude distributions for the two remaining frequencies ($n = 3, 4$) are oscillatory, which indicates that the induced waves in the boundary layer simultaneously contain multiple wave modes. The oscillations in the wave amplitude curves are caused by a wave modulation of two or more independent waves.

Figure 14(b) shows the amplitude development along the cone surface for the next group of three frequencies at $n = 7, 8, 9$ (table 1). The three frequencies vary from 104.5 kHz to 134.3 kHz. There is strong amplitude growth near the exit of the current computational domain for these three frequencies although there is oscillation in amplitudes caused by modulation between different waves. Figure 14(c) shows that there are very strong oscillations in amplitude development along the cone surface for two different frequencies with $n = 10, 11$. Meanwhile, there are clear amplitude amplifications for more higher frequencies with $n = 12, 13, 14, 15$.

The different developments of boundary-layer disturbances induced by free-stream acoustic waves with different frequencies can be explained after the main components of boundary-layer disturbances are identified in the next section.

7.2. Wave-mode identification and comparison with LST results

In the numerical simulation, the receptivity results of 15 independent frequencies are simultaneously obtained. The results of the LST are used to identify different dominant wave modes induced in the boundary layer by the free-stream fast acoustic waves. In this paper, the results of the comparison analyses on the phase velocity, streamwise wavenumber and wave structure for three representative frequencies are presented here. These three frequencies are: 74.61 kHz ($n = 5$), 119.4 kHz ($n = 8$) and 223.8 kHz ($n = 15$). For other frequencies, the results of the comparison between the numerical simulation and LST are very similar to those of the three representative frequencies. In addition, only streamwise wavenumbers are compared with the LST results at four different locations with $x = 10, 50, 172$, and 272 , respectively, for all 15 independent frequencies.

The evolution of the amplitudes of surface pressure perturbations $|p_n(x, y)|$ along the wall surface owing to the free-stream acoustic waves at these three frequencies are redrawn in figure 15. The phase velocities of the induced boundary-layer disturbances obtained from the numerical simulation are calculated based on the phase angles of the pressure perturbations on the wall surface by using (20) and (16). At each frequency, the induced boundary-layer disturbances can be identified by comparing the wavenumbers, the phase velocities, and wave structures from simulation with the eigenvalues and eigenfunctions obtained from the corresponding LST calculations.

Wave fields at 74.61 kHz ($n = 5$)

The development of wave components at a relatively low frequency of 74.61 kHz ($n = 5$ and $F = 45.2$) is first considered. At this frequency, figure 13 shows that the Mack modes become unstable at the surface station of $s = 165$ ($R = 2349.3$), where the instability waves belong to the first Mack mode. As shown in figure 15, at this frequency, the amplitudes of the induced pressure disturbances in the boundary layer increase initially until reaching a peak located approximately at the station of $x = 109.2$. After a decay between the stations of $x = 109.2$ and $x = 200$, the disturbances at this frequency begin to grow and decay again. The behaviours of the induced waves at this frequency can be understood by the comparison with the LST results at the same frequency.

Figures 16(a) and 16(b) compare the streamwise wavenumbers and phase velocities of the induced boundary-layer disturbances at $f^* = 74.61$ kHz between the numerical simulation results and the LST calculations. The LST results include those of the Mack modes and mode I. These two figures show that, at this frequency, in most parts of the cone surface, there is a good agreement in the streamwise wavenumbers and the phase velocities between the induced boundary-layer disturbances and the mode I waves. The induced waves at this frequency have very different wavenumbers and phase velocities from those of the Mack modes. Figure 16 also shows that, near the nose region, the numerical solutions of the disturbance waves have about the same phase velocity as that of the forcing fast acoustic wave. As the induced waves propagate downstream, the phase velocities of the disturbance waves gradually decrease, agreeing very well with the phase velocities of the mode I waves. This agreement indicates that mode I waves, other than the Mack mode waves, are generated inside the boundary layer at this frequency. This is a natural consequence of the mode I waves being synchronized with the forcing fast acoustic waves in the nose region. The wave synchronization results in resonant interaction between mode I and the forcing acoustic waves, which leads to generation and amplification of mode I waves in the boundary layer.

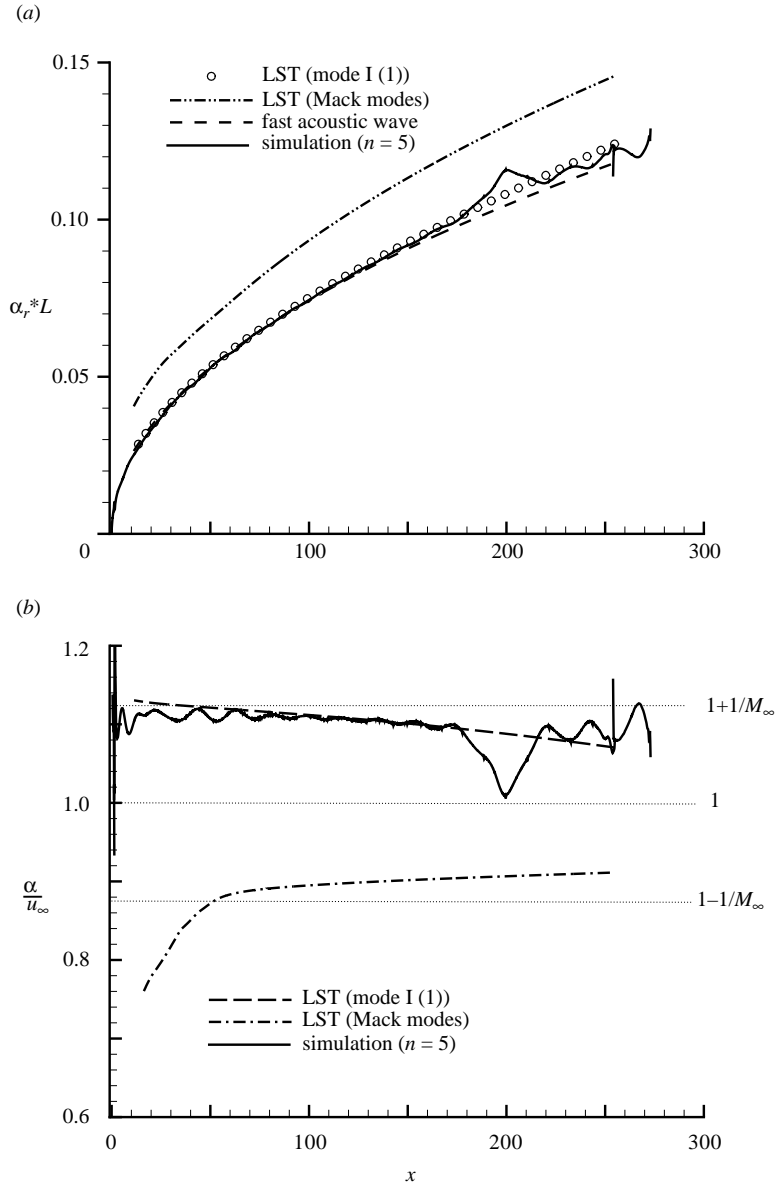


FIGURE 16. Comparison of (a) the streamwise wavenumbers and (b) phase velocities of the induced boundary-layer disturbances obtained by the current simulation with those of mode I and the Mack modes obtained by LST ($n = 5$ and $f^* = 74.61$ kHz).

To confirm the conclusion that mode I waves at 74.61 kHz are generated in the nose region, profiles of the induced disturbances obtained by a temporal Fourier analysis of the simulation results at $x = 109.2$ are compared with the LST results of the corresponding eigenfunctions of mode I and the first Mack mode. The location of $x = 109.2$ is near the peak of mode I amplitudes generated directly by the forcing waves. The real and imaginary parts of the pressure and temperature perturbations, which are calculated by (21) and (22) for temperature perturbations, are compared in

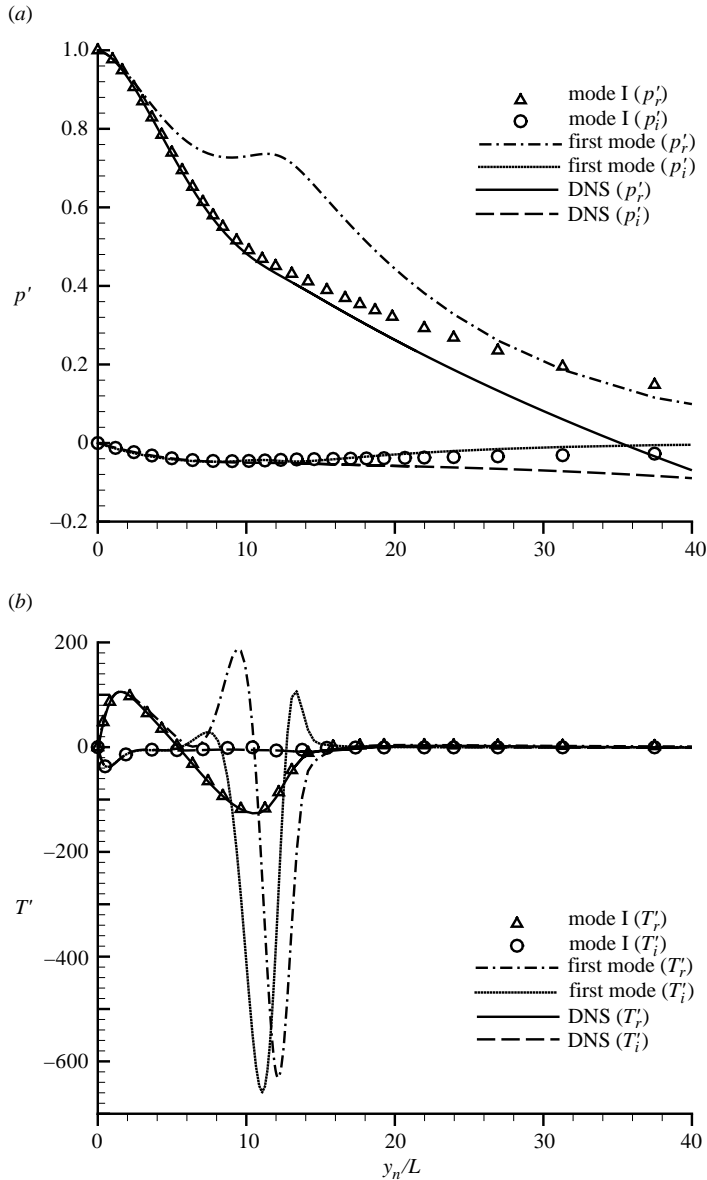


FIGURE 17. Comparison of the real and imaginary parts of pressure and temperature perturbation profiles of the induced boundary-layer disturbances obtained by the current simulation with those of mode I and the Mack modes obtained by LST at $x = 109.2$ ($n = 5$ and $f^* = 74.61$ kHz).

figure 17. In these figures, boundary-layer disturbance results are normalized by non-dimensional pressure perturbations on the wall at the same location. The figures show that the structures of the induced disturbances from the numerical simulation match very well the structures of mode I wave from the LST inside the boundary layer. The thickness of the boundary layer is about $12L^*$ at this station. There are visible

differences in the pressure perturbation structures outside the boundary layer because there are forcing acoustic waves components in the simulation results. Figure 17 shows very significant differences between the numerical simulation profiles and those of the first Mack mode in the region around the edge of the boundary layer. Though not shown here, there are also very good agreements in the wave structures between the simulation results and those of the mode I waves predicted by LST for other variables. Meanwhile the eigenfunctions of the first Mack mode and those of the numerical simulation are very different. Based on the comparisons of phase velocities, wavenumbers, and perturbation eigenfunctions, it is clear that the induced disturbances in the boundary layer at this frequency are not the first Mack-mode waves, but are mainly mode I waves. The mode I waves are generated by their resonant interactions with the forcing acoustic waves.

Figure 17 also shows that the wave structures of mode I are very different from those of the first Mack mode. While there is only one peak in real parts of pressure perturbations in mode I, there are two peaks for the first Mack mode. Furthermore, there are very strong wave amplitudes in the profiles of temperature disturbances for the first Mack mode near the edge of the boundary layer (around $12L^*$), but such a phenomenon does not exist in the profiles of mode I. These characteristics of the wave structures of different normal modes can be used to identify induced boundary-layer disturbances by forcing waves. It should be noted that mode I waves can only be distinguished from the first Mack mode waves in this way before these two modes are synchronized with each other at a downstream location. At the synchronized location between mode I and the Mack modes at a downstream location, it can be shown that the two families of wave modes have almost the same wave structures.

Having identified the induced disturbances in the boundary layer being mode I waves at the frequency of $n=5$, the growth and decay of induced boundary-layer disturbances at this frequency shown in figure 15 can be explained by using the LST results. Although mode I is stable, based on the LST results, figure 15 shows that the induced mode I waves at this frequency are amplified before reaching a peak value in amplitudes at $x=109.2$. The growth of the stable mode I waves in the receptivity process can be explained by using the distribution of streamwise wavenumbers and phase velocities of mode I waves shown in figure 16. From these two figures, the wavenumbers and phase velocities of mode I waves are almost the same as those of the forcing fast acoustic waves near the nose. Owing to the synchronization between mode I waves and the fast acoustic waves near the nose, mode I waves are generated by means of resonant interactions between these two waves. Though predicted to be always stable by LST, mode I waves are amplified before reaching the peak amplitude as a result of their resonant interactions with the fast acoustic waves. As the induced mode I waves propagate downstream, their phase velocities gradually decrease while those of the forcing acoustic waves remain relatively unchanged. Hence, the differences between the two sets of phase velocities increase. When the phase velocities of the mode I waves decrease to a certain value, there are no more resonant interactions between mode I waves and the forcing acoustic waves. Consequently, the amplitudes of the mode I waves decay owing to their inherent stable properties after they reach the peak amplitude at $x=109.2$. Meanwhile, the modulation between mode I waves with the forcing acoustic waves and other waves leads to the secondary growth of mode I waves with the peak amplitude located at $x=233$ (figure 15, $n=5$). Such modulation also results in the oscillation of phase velocities further downstream, which is shown in figure 16.

Based on McKenzie & Westphal's (1968) theory on interaction between disturbance waves and oblique shock waves, slow acoustic waves should be produced by the interaction of the incoming disturbance with the bow shock. However, we found that the phase velocity of disturbances immediately behind the shock is close to that of fast acoustic waves based on our numerical simulations. Therefore, acoustic waves generated behind the shock by free-stream disturbances are either pure fast acoustic waves or dominated by fast acoustic waves. Slow acoustic waves are negligible. Therefore, there is no, or negligible, first mode generated by slow acoustic waves through resonant interactions.

Wave fields at 119.4 kHz ($n = 8$)

The development of wave components at a higher frequency of 119.4 kHz ($n = 8$ and $F = 72.3$) is considered next. Figure 15 shows that, at this frequency, the amplitudes of the induced disturbances in the boundary layer increase initially, reach a peak approximately at the surface station of 30 nose radii, and decay afterward. In the following region between the surface station of 65 nose radii to approximately 190 nose radii, the amplitudes of the disturbance waves stay at an approximately constant level with slight fluctuations. The wave amplitudes increase dramatically in the region downstream of the surface station at $s = 192$.

Again, the results of LST analysis are used to identify the dominant normal modes included in the boundary layer at different locations for disturbances at this frequency. At first, the distributions of streamwise wavenumbers and phase velocities of the induced boundary-layer disturbances at this frequency are compared with those of different normal modes obtained by LST. The comparisons are presented in figure 18. Similar to the results shown in figure 11, there is a gap in the streamwise wavenumber and phase velocity curves for mode I obtained by the LST calculations. The wavenumbers and the phase velocities of the numerical solutions of the induced waves in the boundary layer are compared with those of mode I and the second Mack mode predicted by LST calculations. Figure 18 shows that the streamwise wavenumbers of the induced waves are very close to those of mode I waves in the early region of $x < 66$, which indicates that the induced boundary-layer disturbances are dominated by mode I waves in this region. These mode I waves are generated by their resonant interactions with the forcing fast acoustic waves near the nose. The fact that the induced waves in this region are dominated by the mode I waves can be verified by comparing the wave structures of the numerical simulation with the eigenfunctions of mode I waves obtained from LST. It is found that the structure of induced wave modes in the receptivity simulation agree very well with those of mode I. The comparisons between disturbance structure with the eigenfunctions of the mode I waves from the LST at this frequency are not presented here because they are very similar to the results shown in figure 17 for the case of $n = 5$.

Ma & Zhong (2002, 2003a, b) showed that there exists similarity in development of mode I waves for different frequencies if non-dimensional frequency ω defined in (14) is used. This observation also applies to the current case. For the two frequencies of $n = 5$ and $n = 8$ discussed so far, the locations of mode I waves reaching their respective peak amplitudes are $x = 37.1$ for $n = 8$ and $x = 109.2$ for $n = 5$. The corresponding values of the non-dimensional frequencies ω can be calculated as:

$$\begin{aligned}\omega &= 0.083 \text{ for frequency of } n = 8, \\ \omega &= 0.087 \text{ for frequency of } n = 5.\end{aligned}$$

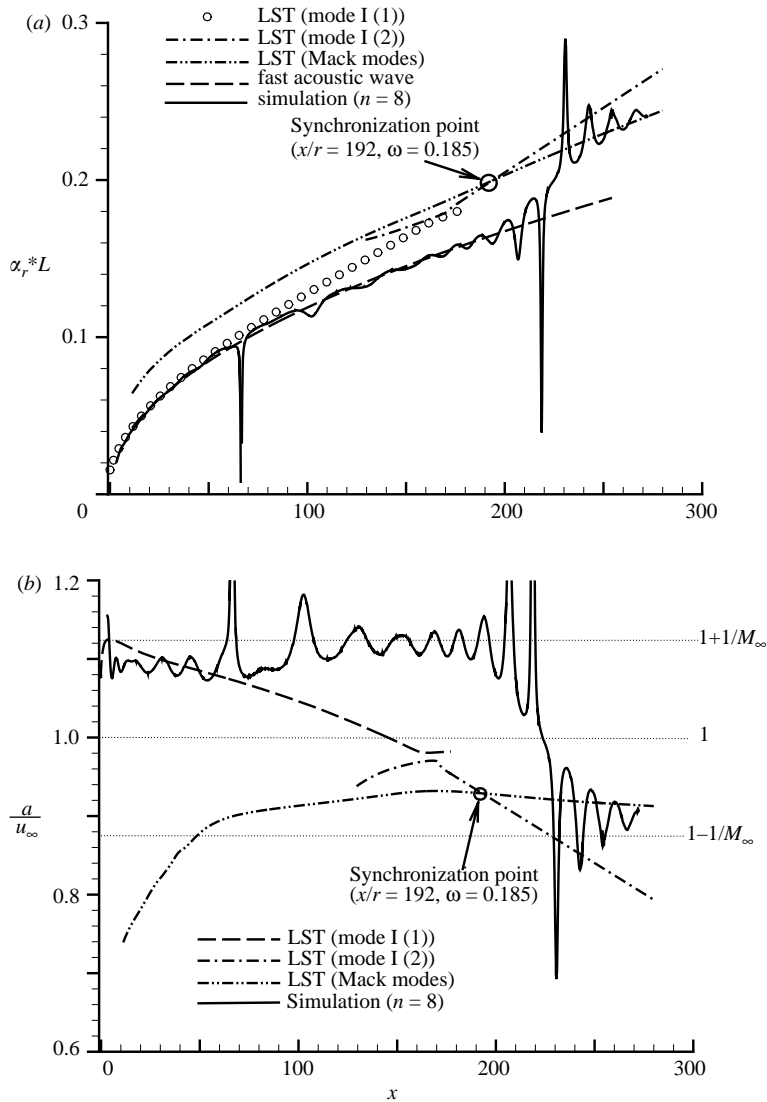


FIGURE 18. Comparison of the wavenumbers and phase velocities of the induced boundary-layer disturbances obtained by the current simulation and those of mode I and the Mack modes obtained by LST ($n = 8$ and $f^* = 119.4$ kHz).

These two computed values of ω are very close to each other, which also demonstrates that the waves in these two frequencies in the early surface locations are indeed mode I waves. This comparison also indicates the similarity in wave patterns of the growth and decay of mode I waves at different frequencies when the distributions are scaled by ω . Again, for the current frequency at $n = 8$, the resonant interactions between the mode I waves inside the boundary layer and the fast acoustic waves outside the boundary layer result in the amplification of the induced boundary-layer disturbances in the region of $x < 37.1$.

Meanwhile, the modulation between the mode I waves and the fast acoustic waves, and the stable properties of mode I waves can explain the growth and decay of

boundary-layer disturbances during their propagation downstream in the region between $37.1 < x < 192$ (figure 15). The wave modulation also leads to strong fluctuations in the distribution of amplitudes of the boundary-layer disturbances in the same region as shown in figure 18. At the earlier surface stations ($x < 66$), this kind of amplitude fluctuation is around the streamwise wavenumbers of mode I, when the components of mode I waves included in boundary-layer disturbances are relatively strong. In the subsequent region ($66 < x < 192$), the modulation of wave modes is around the phase velocity of the fast acoustic waves, which indicates the relative dominance of the fast acoustic waves in boundary-layer disturbances in this region.

In the downstream region of $x > 200$, the boundary-layer disturbances at the frequency of $n = 8$ are strongly amplified, as shown in figure 15. From the distributions of the streamwise wavenumber and phase velocity curves shown in figure 18, the wavenumbers and phase velocities of the induced boundary-layer disturbances match those of the second Mack mode in the region after the 250 surface station, which indicates that the second Mack mode is dominant in this region.

The identification of induced Mack-mode waves is confirmed by comparing the disturbance structures of the numerical simulation with the eigenfunctions of the second Mack mode obtained by LST. Figure 19 shows the comparisons of the eigenfunctions for the pressure and temperature perturbations, respectively, at the surface station of $x = 271$. There is a good agreement in the wave structures between the numerical simulation results and those of LST for the second Mack mode. The slight differences in the comparison are due to there being other weak wave components, such as the forcing fast acoustic waves, in the boundary-layer disturbances besides the second-mode waves. Nevertheless, it is evident that the induced perturbations at this frequency in the boundary layer are dominantly the unstable second Mack mode at this surface location. Having verified that the second Mack-mode waves are the dominant waves inside the boundary layer at the surface region downstream of the 200 nose radii station, it is not difficult to understand the strong amplification of induced boundary-layer disturbances because of the instability of the second Mack mode waves. The growth rates of boundary-layer normal modes at frequency at $n = 8$ from the LST are shown in figure 20. At this frequency, the second-mode Branch I neutral stability point is located at $x = 143.4$. The second Mack-mode waves become unstable in the region of $x > 143.4$. In addition, the growth rates of the second-mode waves reach peak value of $\alpha_i = -0.0051$ at $x = 234$. However, there are no amplified second-mode waves at the frequency of $n = 8$ (figure 15) between $143.4 < x < 192$. On the contrary, the amplitudes of boundary-layer disturbances decay slightly in this region. Therefore, the generation of the second-mode waves does not coincide with the Branch I neutral stability point. As shown in figure 18, the phase velocities of the Mack mode are much lower than those of the forcing fast acoustic waves. Thus, there is no direct interaction between the Mack-mode waves and the forcing fast acoustic waves. Instead, mode I waves serve as a ‘bridge’ in wave interactions in the sense that they can interact with both the Mack modes and the fast acoustic waves. During their propagation downstream, mode I waves generated by fast acoustic waves reach the synchronization point between mode I waves and Mack-mode waves located at $x = 192$ ($\omega = 0.185$). Here, the location of the synchronization point in terms of ω is very close to that shown in figure 11 with $\omega = 0.1825$ at the station $s = 175$ (or $x = 172$) where the local Reynolds number Re is fixed while the frequency varies. At this synchronization point, both mode I and the Mack mode have very similar profiles of eigenfunctions and the same phase velocity. As a result, the mode I waves convert to the Mack-mode waves through resonant interactions. Because the Mack-mode waves are much

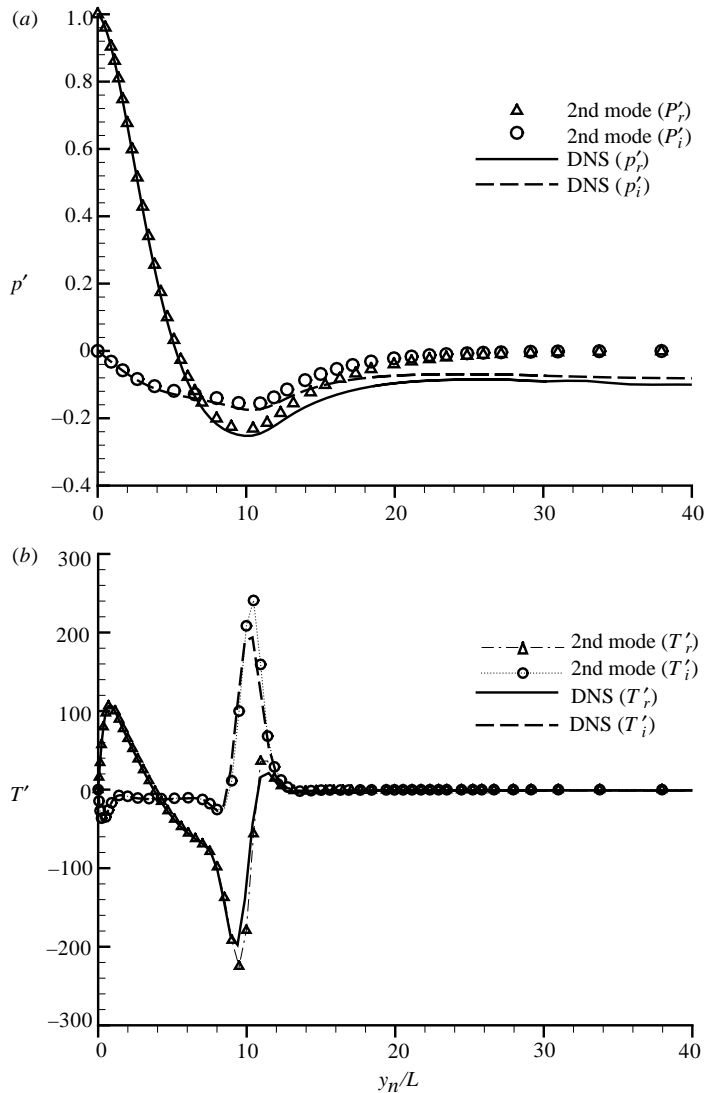


FIGURE 19. Comparison of the real and imaginary parts of pressure and temperature perturbation profiles of the induced boundary-layer disturbances obtained by the current simulation with those of the second Mack mode from the LST at $x = 271$ ($n = 8$ and $f^* = 119.4$ kHz).

more unstable than the mode I waves as shown in figure 20, the amplitudes of the second Mack waves grow significantly afterward. Because the second Mack-mode waves are generated by the mode I waves at the synchronization point, there is no amplification of the second-mode waves in the region before this point, even though the second Mack-mode unstable region begins much earlier. After the generation of the second-mode waves, the boundary-layer disturbances are significantly amplified resulting from the unstable property of the second mode in the downstream region with $x > 192$, which is shown in figure 15. The receptivity mechanism of the second Mack mode to free-stream fast acoustic waves is consistent with the conclusion of our previous study on receptivity of supersonic flow over a flat plate (Ma & Zhong 2003b).

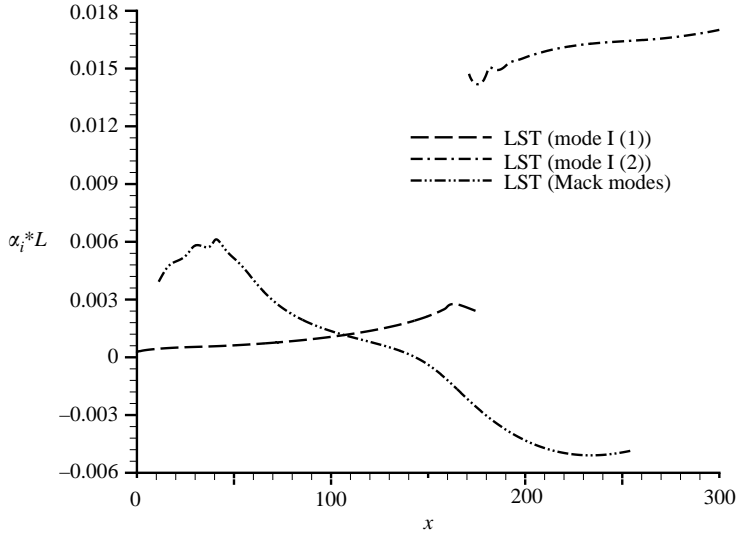


FIGURE 20. Distribution of growth rates of boundary-layer normal modes at the frequency of 119.4 kHz ($n = 8$).

The second mode is generated by its resonant interactions with the mode I waves, which in turn are generated by the forcing fast acoustic waves in the nose region through separate resonant interactions. Such a receptivity mechanism based on the resonant interactions between the forcing waves and various boundary-layer wave modes is very different from those of the subsonic boundary layers. The resonant interaction mechanism also explains why the second Mack mode is not generated in the boundary layer before the synchronization point between mode I and the second mode ($x = 192$), even though the second Mack mode becomes unstable at the earlier surface stations of the 143.4 nose radii. Therefore, the synchronization locations between mode I and the Mack modes shown in figure 13 are important in hypersonic boundary-layer receptivity studies. For this reason, the synchronization location curve is drawn in figure 13 together with the neutral stability curve of the Mack modes. The current receptivity results demonstrate the importance of the receptivity studies in transition prediction because the initial wave generation determines the amplitudes of the subsequent growth of an instability wave.

Having identified the main wave modes included in boundary-layer disturbances owing to forcing fast acoustic waves, the process of receptivity can be demonstrated in the change of wave patterns in the flow field. The wave patterns in the flow field can be represented by contours of real or imaginary parts of the temperature perturbations from a temporal FFT analysis of the simulation results. The real and imaginary parts of the temperature perturbations can be calculated by

$$\text{Re}(T_n(x, y)) = |T_n(x, y)| \cos \phi_n(x, y), \quad (21)$$

$$\text{Im}(T_n(x, y)) = |T_n(x, y)| \sin \phi_n(x, y), \quad (22)$$

where $T_n(x, y)$ and $\phi_n(x, y)$ are amplitudes and phase angles of the temperature perturbations of frequency f_n computed by (18). Figure 21 shows the contours of the real part of the temperature perturbations in the whole computational flow field for the frequency of $f^* = 119.4$ kHz ($n = 8$). The long computational domain is divided into nine sections in order to present the details of the wave modes clearly. The

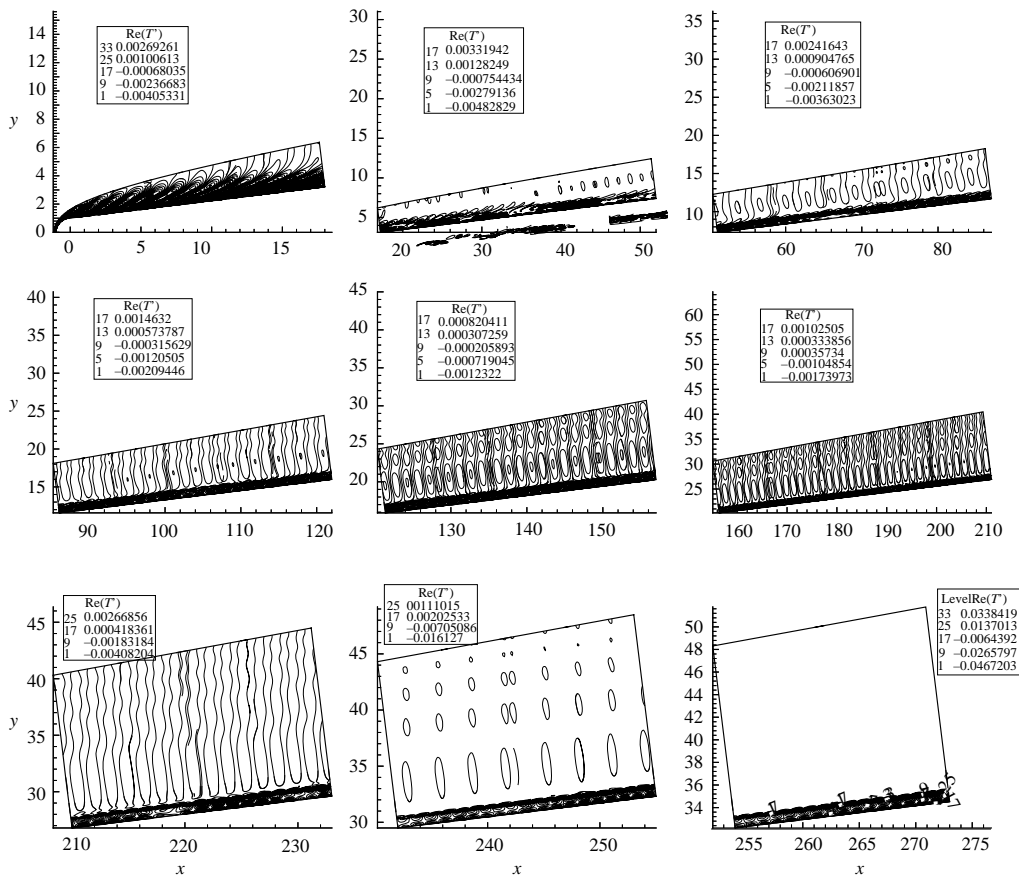


FIGURE 21. Contours of the real parts of the temperature perturbations in the flow field for wave components at $f^* = 119.4$ kHz ($n = 8$).

contours show the development of temperature perturbations of a fixed frequency in the entire flow field, from the nose region to the 273 nose radii surface station downstream. The outer boundary of the computational domain is the bow shock. The interaction of forcing waves with boundary-layer wave modes and the subsequent development of the induced waves can be observed in these figure 21.

In the early region of $x < 20$, figure 21 shows that the forcing waves from the free stream at the frequency of 119.4 kHz pass through the bow shock and enter the boundary layer to generate mode I waves in the boundary layer. The mode I waves are generated by resonant interactions with the forcing waves in this region. In the subsequent region of $20 < x < 60$, mode I gradually becomes less synchronized with the forcing waves. Consequently, it develops and decays along the boundary layer in this region. The disturbance waves in this early region in the boundary layer are dominantly mode I waves, the amplitudes of which become weaker along the surface. The growth and decay of the mode I waves shown in this figure are consistent with the amplitude distribution of this frequency shown in figure 14. In the next region of $60 < x < 200$, the wave modes are a mixture of forcing waves and mode I waves. The fluctuations in the boundary layer in this region remain roughly constant as shown in figure 14. Further downstream, the second Mach mode of this frequency begins to develop. The figure distinctly shows that different wave structures are developed in the

boundary layer. The second mode becomes the dominant waves in the region further downstream at $x > 220$ (see figure 14). In this region, the figure shows a rope wave, which is the signature feature of the second Mack mode, at the edge of the boundary layer. After they are generated, the second mode waves grow rapidly because they are linearly unstable. Though not shown in these figures, the second mode will peak at its Branch II neutral stability point located outside the current computational domain and decays afterward (based on LST prediction).

The main induced wave modes, mode I, mode II and the Mack mode, in the boundary layer can be identified from the simulation results because they have different wave speeds and different structures in their perturbation eigenfunctions. The wavenumbers, wave speeds and perturbation eigenfunctions of each wave mode can be obtained by an LST analysis. Therefore, the wave modes contained in the numerical simulation solutions can be identified by comparing their perturbation patterns with those obtained by LST. Figure 22 shows numerically obtained contours of the real part of the temperature perturbations in three localized regions of the flow field where the perturbations are dominated by one of the three major modes in the boundary layer. Specifically, the figure shows mode I in the region around 170 nose radii at the frequency of $f^* = 119.4 \text{ kHz}$ ($n = 8$), mode II in the region around 261 nose radii at $f^* = 179.1 \text{ kHz}$ ($n = 12$), and the second Mack mode in the region around 261 nose radii at $f^* = 119.4 \text{ kHz}$ ($n = 8$). The wave structures inside the boundary layer are different among these three wave modes. Modes I and II have distinctively different structures from the second Mack mode near the wall. The second Mack mode has a typical ‘rope wave’ structure with strong perturbations at the edge of the boundary layer, while modes I and II have stronger wave amplitudes inside the boundary layer. The wave structures of mode I are slightly different from those of mode II in the middle region of the boundary layer.

Wave fields at 223.8 kHz ($n = 15$)

The development of wave components at a frequency of 223.8 kHz ($n = 15$ and $F = 135.5$) is considered as the high-frequency case. The neutral curve in figure 13 shows that both the first and second Mack modes are always stable at this high frequency. Similar to the previous cases of lower frequencies, the wave modes of the numerical simulation results can be identified by the comparison with the corresponding LST results.

As shown in figure 15, the amplitudes of the induced disturbances at the frequency of $n = 15$ in the boundary layer grow and decay first in a very small mode I region of $x < 9.5$. Figure 23 compares the streamwise wavenumbers and phase velocities of the induced boundary-layer disturbances at this frequency with the real part of eigenvalues of the Mack modes, modes I and mode II from the LST. This figure indicates that, owing to their resonant interactions with the fast acoustic waves, mode I waves are generated near the nose region and amplified in the region of $x < 9.5$. Similar to the previous cases of lower frequencies, the identification of the induced mode I waves in this region can be verified by matching the structures of boundary-layer disturbances from the simulation with those of mode I waves from the LST. The comparisons are not shown here because they are similar to those of the lower-frequency cases presented earlier.

Because the second Mack mode is stable, there should be no amplified second mode at the frequency of $n = 15$. However, figure 15 shows that the amplitudes of another wave mode at this frequency gradually grow during its propagation downstream after $x > 50$. In the region between the surface station of 50 to 230 nose radii, the amplitudes

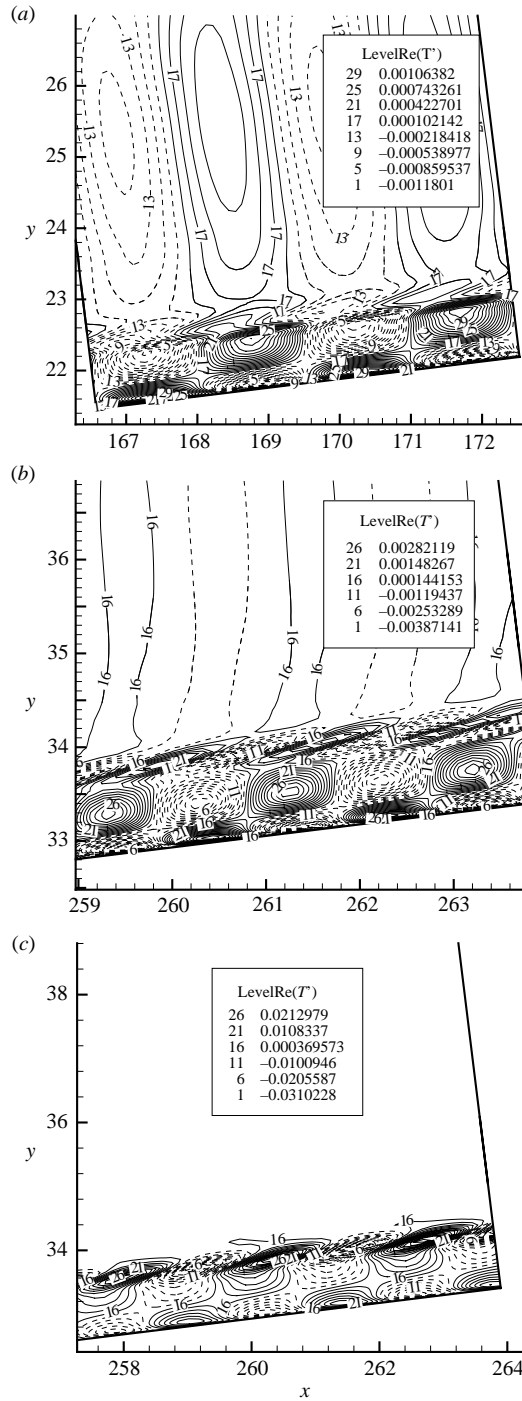


FIGURE 22. Contours of the real parts of the temperature perturbations in three localized regions of the flow field, where the flow fluctuations are dominated by one of the three different modes: (a) mode I at $f^* = 119.4$ kHz ($n = 8$); (b) mode II at $f^* = 179.1$ kHz ($n = 12$); (c) the second Mack mode at $f^* = 119.4$ kHz ($n = 8$).

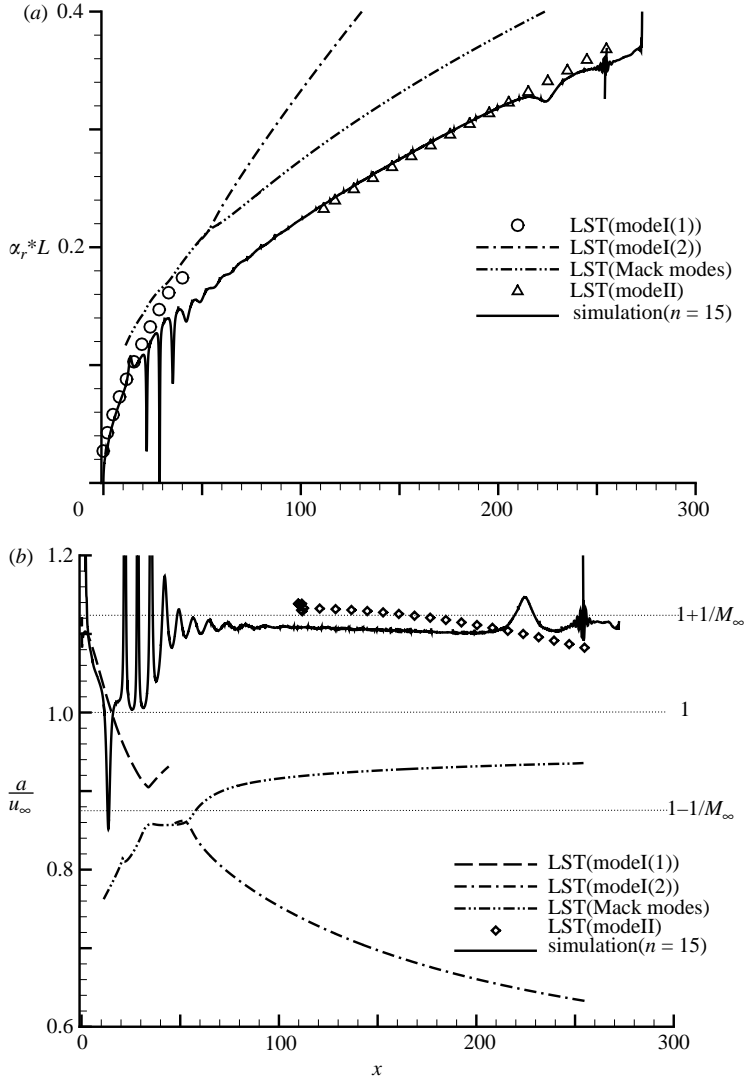


FIGURE 23. Comparison of the streamwise wavenumbers and phase velocities of the induced boundary-layer disturbances obtained by the current simulation with those of mode I, mode II and the Mack modes obtained by LST ($n = 15$ and $f^* = 223.8$ kHz).

of the disturbance waves go through a region of growth and decay, with the peak amplitude located at around 178 nose radii. Figure 23 shows that this wave mode has the same phase velocities and wavenumbers as those of mode II, which indicates that mode II waves are generated by forcing fast acoustic waves.

The identification of the induced mode II waves at the frequency of $n = 15$ in the region of $x > 50$ can be further verified by comparing the perturbation eigenfunctions across the boundary layer at a fixed surface location. Figure 24 compares the wave structures of the induced boundary-layer disturbances at $x = 177.3$ ($R = 2455$) with the eigenfunctions of mode II from the LST. There is a very good agreement in the pressure and temperature perturbations except for visible differences outside the boundary layer. The differences outside the boundary layer are caused by the fact that, in addition to the mode II waves, there are also forcing acoustic wave components in

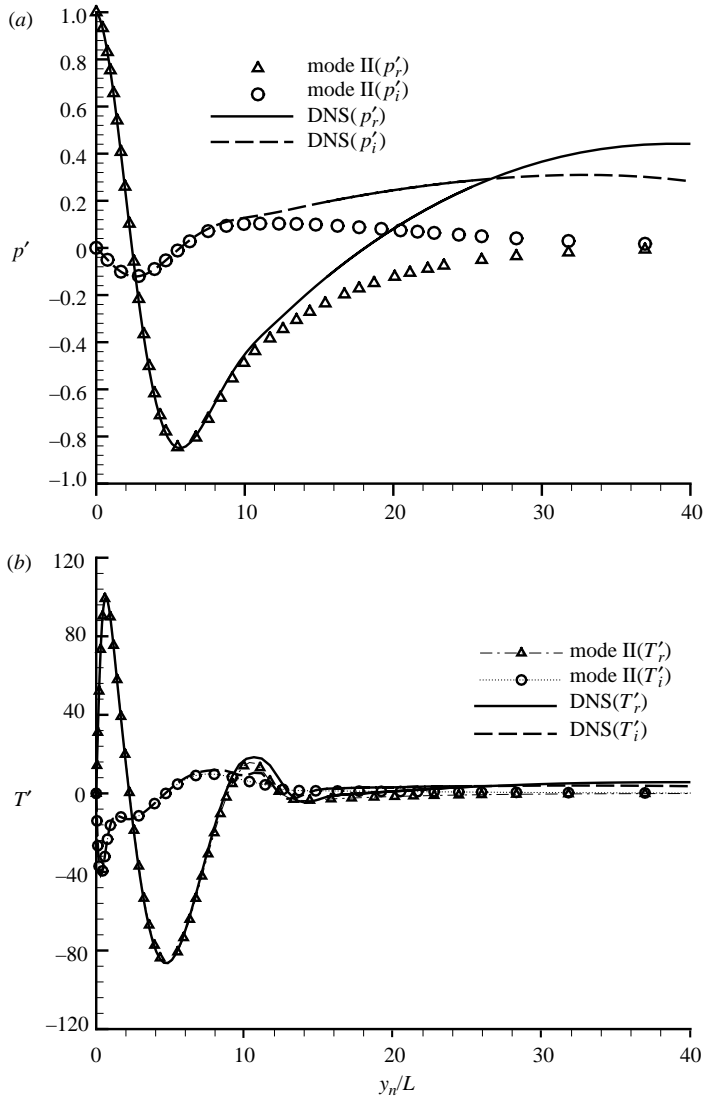


FIGURE 24. Comparison of the real and imaginary parts of pressure and temperature perturbation profiles of the induced boundary-layer disturbances obtained by the current simulation with those of mode II from the LST at $x = 177.3$ ($n = 15$ and $f^* = 223.8$ kHz).

the induced flow field. Similar to the excitation of the mode I waves in the previous cases of lower frequencies, although mode II waves are linearly stable from the LST results, there is a resonant interaction between mode II waves and the fast acoustic waves because their phase velocities are very close to each other, as shown in figure 23. This wave synchronization leads to the amplification of mode II waves. As the induced mode II waves propagate downstream, they eventually decay because their wave velocities gradually decrease and differ from those of the fast acoustic waves. Consequently, the interactions between the mode II waves and the forcing fast acoustic waves gradually become weaker as they propagate downstream. Without the resonant interactions, the induced mode II waves eventually decay because they are linearly stable.

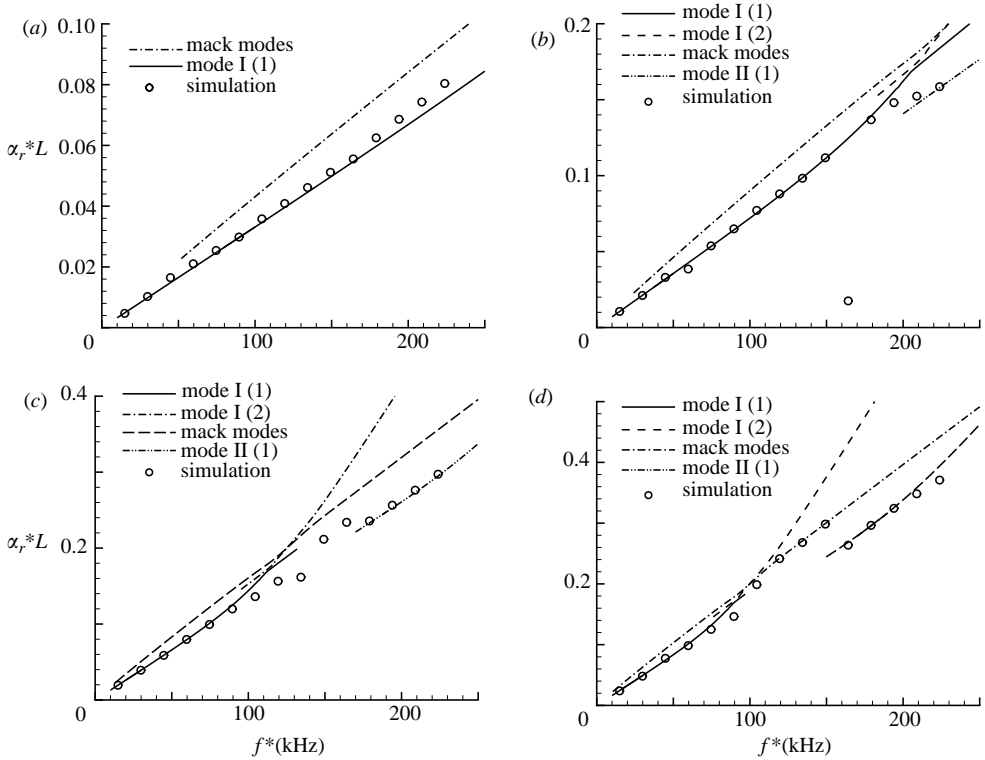


FIGURE 25. Comparison of the wavenumber spectra of the induced boundary-layer disturbances at different frequencies with those of boundary-layer normal modes obtained by LST at four surface stations. (a) $x = 10$, (b) 50, (c) 172, (d) 272.

Wave number spectra

Having identified the dominant induced wave modes in the boundary layer at the three representative frequencies of $n = 5, 8, 15$, it is clear that the induced wave modes are mainly components of the mode I, the second Mack mode, and mode II, depending on the locations and frequencies. The first Mack mode does not appear in the induced wave field. For all 15 frequencies, the receptivity mechanism of the hypersonic boundary layer is the resonant interaction mechanism among the relevant wave modes and the forcing waves. Figure 14 shows the amplitudes of the pressure perturbations on the cone surface for all these frequencies. The induced wave modes of all 15 frequencies can be identified easily by using similar analyses based on comparisons with LST results. Here, the excitations of different boundary-layer wave modes of all 15 frequencies are demonstrated by comparing the streamwise wavenumbers for the current receptivity simulation with the real parts of the eigenvalues of mode I, mode II and the Mack modes from the LST at four different surface locations of $x = 10, 50, 172$ and 272. Figure 25 shows the results of the comparison. Such comparisons can also be used to identify the dominant wave modes for all frequencies as the waves travel through these surface locations.

At the early station near the nose at $x = 10$, figure 25(a) shows that the streamwise wavenumbers of the induced boundary-layer disturbances agree with those of mode I from the LST calculations for most of the 15 frequencies. This agreement indicates that the wave amplitude spectra shown in figure 26 are mode I waves for all of the

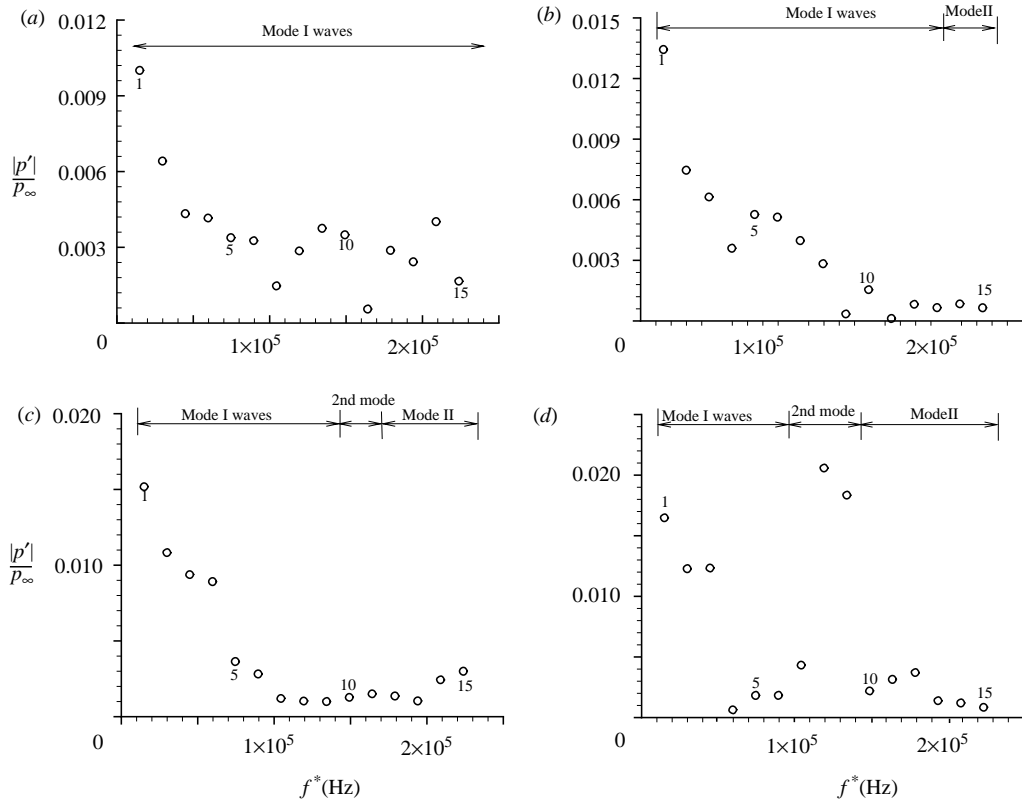


FIGURE 26. Fluctuation spectra of pressure perturbations on the cone surface at four surface locations. The regions of dominant induced waves are marked in the figure. (a) $x = 10$, (b) 50, (c) 172, (d) 272.

15 frequencies. There is a better agreement in the streamwise wavenumbers for lower frequencies with $f_n^* \leq 164.1$ kHz ($n \leq 11$). The agreement at the lower frequencies is better because of the dominance of mode I waves included in the boundary layer at lower frequencies. The visible differences in the wavenumbers at higher frequencies with $n \geq 12$ are due to the modulation of the mode I waves and other wave component inside the boundary layer.

Figure 25(b) compares the wavenumbers of the induced boundary-layer disturbances at different frequencies with the LST results at the surface location of $x = 50$. At this surface location, mode II waves begin to be generated at high frequencies of $n = 14, 15$, while mode I waves are the dominant components for lower frequencies of $n \leq 13$. The deviation of the wavenumber at the frequency of $n = 11$ is due to the modulation of mode I waves with other modes, which is also shown in figure 14 where the total boundary-layer disturbances at $n = 11$ decay to a minimum value at $x = 50$. As the induced mode I waves propagate downstream, starting from higher frequencies, mode I waves decay and mode II waves are generated. No second modes are generated because they are stable modes for the higher frequencies even when there is a synchronization location between mode I and the Mack modes at this surface location. The dominant induced wave modes are marked in figure 26.

At the further downstream location of $x = 172$, figure 25(c) shows that there are more mode II waves generated in the high-frequency band with $n \geq 12$, while mode I

waves are still the main components in the low-frequency band with $n \leq 8$. In the middle-frequency band with $9 \leq n \leq 11$, the second Mack-mode waves are generated by the mode I waves. In fact, boundary-layer disturbances at the frequency of $n = 9$ at this location is in the initial generation region from the mode I waves to the second Mack-mode waves. Because the second modes are unstable in these middle frequencies of $9 \leq n \leq 11$, the second Mack modes become dominant as they propagate further downstream. Therefore, at this surface station, the induced waves are a mixture of the following three modes: mode I, the second Mack mode and mode II. The dominant induced wave modes are also marked in figure 26 in the same surface location.

Figure 25(d) presents the comparison of wavenumber spectra at a still further downstream location of $x = 272$. At this location, there are clearly second-mode waves shown in the middle frequency band of $7 \leq n \leq 10$. At frequencies lower than $n = 7$, mode I waves are dominant, while mode II waves are dominant at higher frequencies with $n \geq 11$. These wavenumber spectra show a very clear picture of the receptivity process that mode I is generated first by their resonant interactions with the forcing acoustic waves. The second Mack mode is then generated by the mode I waves through separate resonant interactions when mode I propagates downstream. There are significant second Mack mode components through the resonant interaction only when the second mode is unstable in the region of resonant interactions with mode I. Otherwise, mode II waves are generated by their resonant interactions with the forcing acoustic waves further downstream location. At a fixed location, the induced waves are again a mixture of all three dominant wave modes, which are marked in figure 26 in the same surface location. The first Mack mode is not generated because it does not interact with mode I.

Based on the above discussions, the specific regions of the dominant induced wave modes are marked in figure 26. At surface location of $x = 10$ nose radii, wave modes induced in the boundary layer of all 15 frequencies are dominantly mode I waves. The mode I waves are linearly stable and eventually decay. They are generated and amplified in a local region when they are in resonance with the forcing fast acoustic waves. At a later station of $x = 50$, the waves of lower frequencies are still dominated by mode I waves, but mode II waves begin to develop at higher-frequency waves. At the downstream location of $x = 172$, the mode I wave frequency region continues to decrease. The second mode begins to develop in a small frequency band around 150 kHz. Meanwhile, the induced waves at higher frequencies are dominated by mode II waves. At a further downstream location of $x = 272$, the unsteady second Mack mode has grown substantially in a frequency band around 130 kHz. The second Mack mode becomes dominant instability waves because it is linearly unstable. As the boundary layer becomes thicker at further downstream locations, the frequencies of the most unstable second mode decrease. There are also mode I and II waves at lower and higher frequencies, respectively. Again, there are no first Mack mode components in the boundary layer.

To summarize the LST analysis of the simulation results of the receptivity, it is clear that the synchronization location between mode I and the second Mack mode plays the most important role in the receptivity of the second Mack mode in the boundary layer. In the current hypersonic flow over a blunt cone, the synchronization location is located downstream of the branch I neutral stability location of the second mode. As a result, there are no noticeable second mode components in the region before the synchronization location, even though the second Mack mode is linearly unstable there. Similarly, there are no first Mack mode components generated by the receptivity process because the unstable region of the first Mack mode is upstream of the synchronization location. In addition, owing to the resonant interactions with the

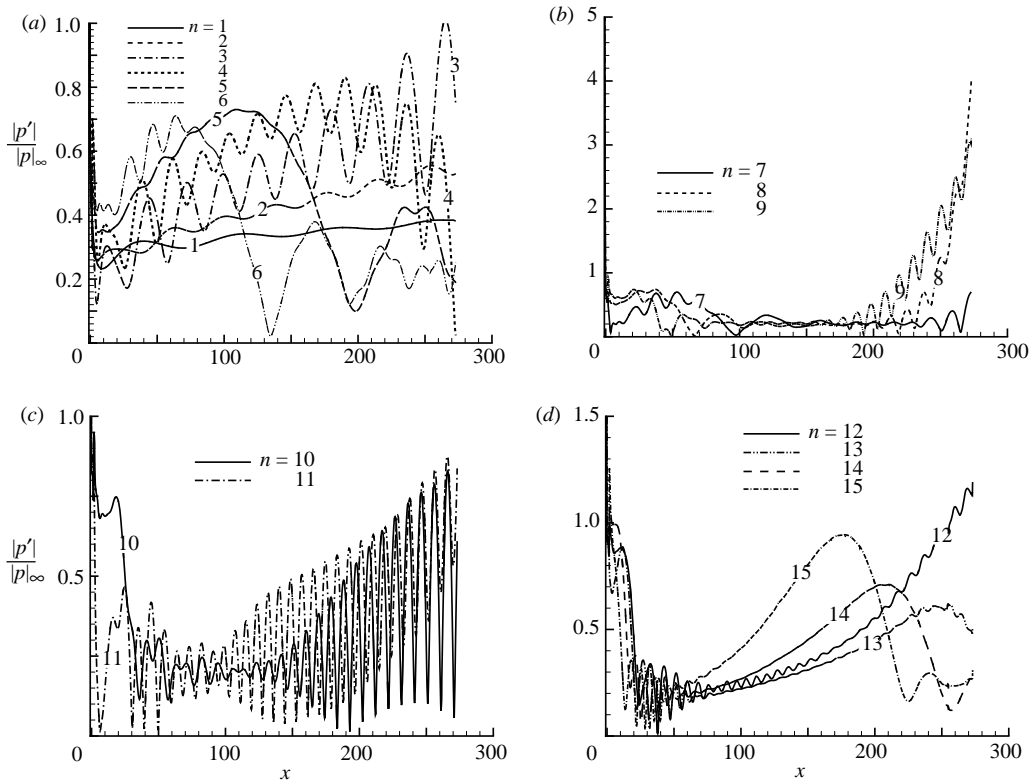


FIGURE 27. Pressure perturbations on the wall normalized by amplitudes of the pressure perturbations at the same frequency in the free stream.

forcing acoustic waves, there is amplification of the mode I waves in the early region near the nose and amplification of the mode II waves in the region downstream. The mode I and mode II waves grow owing to their respective resonant interactions with the forcing waves, even though these two modes are always stable.

Overall, the receptivity mechanisms of the current axisymmetric hypersonic boundary layer over a blunt cone are very different from those of the incompressible boundary-layer flow. The resonant interactions between the forcing waves and the boundary-layer wave modes, and the resonant interactions among the boundary-layer normal modes, are the main mechanisms of the excitation of the unstable Mack modes in the hypersonic boundary layer over a blunt cone.

7.3. Response coefficients

Figure 14 shows that the boundary-layer receptivity is strongly dependent on the wave frequencies. In order to simulate the free-stream disturbances of Stetson *et al.* wind-tunnel experiments by the current numerical simulation, the amplitudes of free-stream forcing fast acoustic waves are not the same for different frequencies (table 1). Consequently, the perturbation amplitudes shown in figure 14 do not accurately reflect the frequency effects on the receptivity because of different forcing wave amplitudes at different frequencies. In order to obtain the frequency effect on the receptivity, the pressure perturbations of the induced boundary-layer disturbances of a given frequency are normalized by the amplitudes of the pressure perturbations at the same frequency in the free stream. Figure 27 shows the profiles of the normalized amplitudes

of pressure perturbations along the wall as functions of the x -coordinate. Overall, the amplitudes of pressure perturbations in the computational domain induced by free-stream fast acoustic waves are less than 4 when they are normalized by amplitudes of free-stream forcing acoustic waves of the same frequency. Maximum receptivity is obtained at the frequency of $n = 8$ owing to the growth of the unstable second-mode waves after they are generated by the mode I waves. These figures show that the growth of the mode I and mode II waves for different frequencies are in the same order of magnitudes (around 1.0) because they are generated by the same mechanism of resonant interactions with the forcing acoustic waves. On the other hand, the second mode growth is much stronger because the second modes are linearly unstable after they are generated by the receptivity process.

In a boundary-layer receptivity study, a receptivity coefficient, which is defined as the ratio of the amplitude of the induced second-mode wave at the Branch I neutral stability point to that of the forcing free-stream disturbance waves, is usually used to quantitatively describe the strength of the receptivity (Saric *et al.* 2002). However, for hypersonic boundary receptivity, as discussed earlier in this paper, there are no second Mack mode waves generated by free-stream fast acoustic waves at the Branch I neutral point by the receptivity process. Instead, the second Mack mode waves are generated by the mode I waves at the synchronization point between mode I and the second mode. The synchronization point between mode I and the second mode for the current Mach 7.99 flow over a blunt cone is located downstream of the Branch I neutral stability point (figure 13). Therefore, a response coefficient is used in this paper to quantitatively study the acoustic receptivity of the boundary layer. Specifically, the response coefficient of the boundary layer to forcing disturbances for a given mode is defined as

$$K_{mode} = \frac{|p'_{mode}|}{|p'_{\infty}|}, \quad (23)$$

where $|p'_{mode}|$ is the maximum amplitude of pressure perturbations for the given wave mode, which includes mode I, mode II and the second Mack mode. The response coefficients can be used to measure the maximum responses of a given wave mode to forcing disturbances. For the second Mack mode, this maximum value is located at the Branch II neutral point, which is outside the computational domain of the current simulation. Therefore, the response coefficients for the second Mack mode are not available in this study. Since the response coefficients are not the same as the commonly used Branch I receptivity coefficient used in the literature (Saric *et al.* 2002), they are termed the response coefficients in this paper.

In the upstream region near the nose, the disturbance waves are dominated by mode I waves for different frequencies. Response coefficients of mode I waves are obtained for frequencies with $n \leq 10$. The locations of peak mode I waves move upstream toward the nose when frequencies increase. For higher frequencies with $n \geq 11$, the locations of the peaks of amplitudes for the mode I waves are so close to the junction between the spherical nose and cone that the growth of mode I waves is affected by the effect of discontinuity in surface curvature at the junction. Therefore, the response coefficients defined in (23) are not available for higher frequencies of $n \geq 11$. From figure 27, mode II waves reach local peak values for frequencies with $n = 13, 14, 15$. The amplitude peaks for mode II perturbations at lower frequencies are not available in this study because they are located outside the current computational domain. At low frequencies with $n \leq 6$, the second-mode waves will appear in the region outside the current computational domain. In the frequency band of $7 \leq n \leq 9$, the second

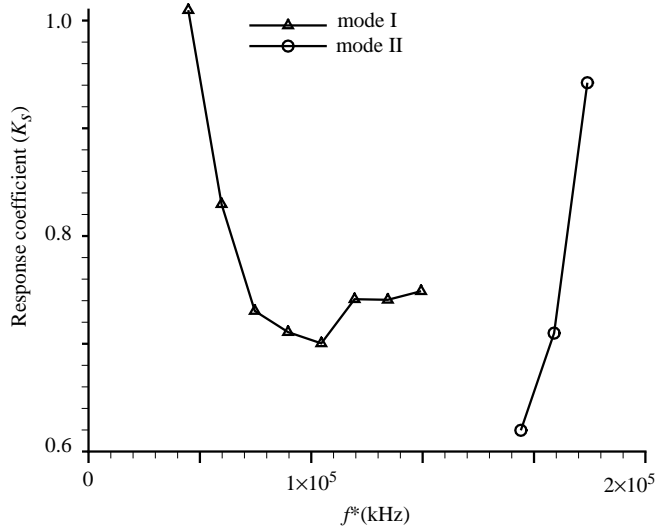


FIGURE 28. The response coefficients of mode I waves and mode II waves at different frequencies.

modes are generated in the simulation, but their Branch II neutral points are located outside the current computational domain. For frequencies with $n = 10$ or $n = 11$, the induced second-mode waves are strongly modulated by other wave components inside the boundary layer. As a result, the peak second-mode waves are difficult to determine from the simulation results. For still higher frequencies, the second Mack modes are always stable. No significant second mode components are found in the receptivity simulation results. Therefore, only response coefficients of mode I waves and mode II waves are presented in this paper.

Figure 28 shows the response coefficients of the mode I waves and mode II waves at different frequencies. Overall, the magnitudes of the response coefficients of mode I and mode II waves are of the order of 1 for different frequencies. From our previous study on receptivity of a sharp flat-plate boundary layer to free-stream fast acoustic waves (Ma & Zhong 2002, 2003a, b), the response coefficients of mode I and mode II waves decrease with increasing frequencies. This trend is also true for mode I response coefficients at frequencies with $n \leq 7$. However, figure 28 shows that the response coefficients of mode I waves or mode II waves increases with increasing frequencies after $n \geq 8$.

8. Summary and conclusions

The receptivity of Mach 7.99 flow over a 7° half-angle blunt cone, corresponding to Stetson *et al.*'s boundary-layer stability experiments, has been studied in this paper by numerical simulation. Even though there is still a discrepancy in growth rates of the second mode between the current numerical results and the experimental results of Stetson *et al.*, it brought out some new physics on receptivity that has never been documented in experiments.

Both steady base flow and unsteady flow solutions of the receptivity process have been calculated by using a fifth-order finite-difference shock-fitting method to solve the full Navier-Stokes equations. Fast acoustic waves at a range of frequencies are

imposed in the free stream in front of the bow shock as forcing waves in the unsteady flow simulation.

The current steady-flow solution of the full Navier-Stokes equations agrees very well with those computed by Herbert & Esfahanian (1993) by using the thin-layer Navier-Stokes equations. In addition, the current solution agrees well with Stetson *et al.*'s experimental results on surface pressure, bow shock locations, and tangential velocities outside the boundary layer. The steady base flow solution demonstrates the effects of the entropy layer on the steady flow field. The entropy layer is created at the bow shock, initially outside the boundary layer near the nose region. The presence of the entropy layer creates an additional generalized inflection point in the region outside the boundary layer. The entropy layer is gradually merged with the boundary layer as it is convected downstream. Eventually, it is swallowed by the boundary layer at a surface location of approximately 60 nose radii for the current flow. Further downstream, the boundary-layer profiles gradually approach the same flow over a sharp cone.

Having obtained the steady base flow solution, the receptivity to free-stream fast acoustic waves is investigated by numerical simulation. A total of 15 frequencies have been considered in the receptivity simulation. The unsteady simulation results show a complex development of wave modes induced in the boundary layer by the free-stream acoustic waves. The wave modes induced in the boundary layer by the receptivity process are identified by comparison with the corresponding LST results. It is found that the basic receptivity mechanisms of the current axisymmetric hypersonic flow over a blunt cone are resonant interactions between the forcing waves and boundary-layer wave modes, and resonant interactions among different boundary-layer wave modes. Depending on the surface region and wave frequency, the disturbance waves induced in the boundary layer contain mode I, mode II and the second Mack mode waves. The wave structures obtained from the simulation are compared with those obtained from the LST for mode I, mode II and the second mode. Very good agreement was obtained for each frequency at a region where one of the wave modes is expected to be dominant.

Through comparison with the LST results, it is found that the synchronization between mode I and the second mode plays the most important role in the receptivity of the second Mack mode in the boundary layer. Specifically, mode I waves are generated first by the forcing fast acoustic waves by their mutual resonant interactions. As the induced mode I waves propagate downstream, they are synchronized with the second Mack mode. The resonant interactions between mode I and the second Mack mode at the synchronization location lead to the generation of the second Mack mode. In the current flow over a blunt cone, the synchronization location is located downstream of the branch I neutral stability location of the second mode. As a result, there are no noticeable second mode components in the region before the synchronization location, even though the second mode is linearly unstable there. Similarly, there is no first Mack mode components generated by the receptivity process because the unstable region of the first Mack mode is upstream of the synchronization location. Therefore, mode I plays a very important role in the receptivity process. The receptivity mechanism based on resonant interactions leads to the delay of excitation of the second mode in the current hypersonic flow over a blunt cone. This may explain stabilization of the second mode excitation in hypersonic boundary flow by nose bluntness. In addition, owing to the resonant interactions with the forcing acoustic waves, there is amplification of mode I waves in the region near the nose and amplification of mode II waves in the region downstream. The mode I and

mode II waves grow by their respective resonant interactions with the forcing waves even though these two modes are always stable. The results also show the excitation of mode II waves for higher-frequency waves at downstream locations. Overall, the receptivity mechanism is very different from those of the incompressible boundary-layer flow. The resonant interactions between the forcing waves and boundary-layer wave modes and the resonant interactions among these normal modes is the main cause of the excitation of the unstable Mack modes in a hypersonic boundary layer over a blunt cone.

In an effort to investigate the growth rate discrepancy between the LST predictions and those measured in Stetson *et al.*'s experiments, the growth rates of the second Mack mode calculated by LST are compared with experimental results and with those obtained by current numerical simulation. The LST results are consistent with other authors in that they predict much higher growth rates than those measured by Stetson *et al.* The direct numerical simulation in this paper provides an independent comparison with the LST results. It was found that the second Mack mode calculated by the current numerical simulation has the same wave numbers and slightly higher growth rates as the second mode predicted by the LST calculations. Therefore, the current simulation results support the validity of the LST calculations. The disagreements between the LST results and those of the experiments may be due to nonlinear effects in the experimental waves or other reasons. In addition, the non-dimensional phase velocities of the major normal modes (mode I, mode II and the Mack modes), have also been calculated in this paper. Both mode I and mode II originate from the fast acoustic wave limit with an initial phase velocity of the fast acoustic wave. On the other hand, the first Mack mode originates from the slow acoustic wave side with an initial phase velocity. It is found that the distributions of phase velocities for both mode I and mode II for the current hypersonic flow over a blunt cone are discontinuous when they cross the line of the phase velocity of the entropy/vorticity wave.

This work was sponsored by the Air Force Office of Scientific Research, USAF, under AFOSR Grant F49620-00-1-0101, monitored by Dr John Schmisser. The views and conclusions contained herein are those of the authors and should not be interpreted as necessarily representing the official policies or endorsements either expressed or implied, of the Air Force Office of Scientific Research or the US Government.

REFERENCES

- DEMETRIADES, A. 1974 Hypersonic viscous flow over a slender cone. Part III: Laminar instability and transition. *AIAA Paper* 74-535.
- DEMETRIADES, A. 1977 Laminar boundary layer stability measurements at Mach 7 including wall temperature effects. *AFOSR-TR* 77-1311.
- EIBLER, W. & BESTEK, H. 1996 Spatial numerical simulations of linear and weakly nonlinear instabilities in supersonic boundary layers. *Theoret. Comput. Fluid Dyn.* **8**, 219–235.
- ESFAHANIAN, V. 1991 Computation and stability analysis of laminar flow over a blunt cone in hypersonic flow. PhD thesis, The Ohio State University.
- FEDOROV, A. V. 2002 Receptivity of high speed boundary layer to acoustic disturbances. *AIAA Paper* 2002-2846.
- FEDOROV, A. V. 2003 Receptivity of a high-speed boundary layer to acoustic disturbances. *J. Fluid Mech.* **491**, 101–129.
- FEDOROV, A. V. & KHOKHLOV, A. P. 2001 Prehistory of instability in a hypersonic boundary layer. *Theoret. Comput. Fluid Dyn.* **14**, 359–375.

- FEDOROV, A. V. & KHOKHLOV, A. P. 2002 Receptivity of hypersonic boundary layer to wall disturbances. *Theoret. Comput. Fluid Dyn.* **15**, 231–254.
- FEDOROV, A. V. & TUMIN, A. 2001 Initial-value problem for hypersonic boundary layer flows. *AIAA Paper* 2001-2781.
- HERBERT, TH. & ESFAHANIAN, V. 1993 Stability of hypersonic flow over a blunt body. *AGARD CP* 514, pp. 28-1–28-12.
- KUFNER, E. & DALLMANN, U. 1994 Entropy- and boundary layer instability of hypersonic cone flows – effects of mean flow variations. *IUTAM Symp. Laminar–Turbulent Transition, Sendai/Japan, September 1994*, pp. 197–204. Springer.
- KUFNER, E., DALLMANN, U. & STILLA, J. 1993 Instability of hypersonic flow past blunt cones – effects of mean flow variations. *AIAA Paper* 93-2983.
- LEES, L. & LIN, C. C. 1946 Investigation of the stability of the laminar boundary layer in compressible fluid. *NACA TN* 1115.
- MA, Y. & ZHONG, X. 2001 Numerical simulation of receptivity and stability of nonequilibrium reacting hypersonic boundary layers. *AIAA Paper* 2001-0892.
- MA, Y. & ZHONG, X. 2002 Receptivity to free-stream disturbances of Mach 4.5 flow over a flat plate. *AIAA Paper* 2002-0140.
- MA, Y. & ZHONG, X. 2003a Receptivity of a supersonic boundary layer over a flat plate. Part 1. Wave structures and interactions. *J. Fluid Mech.* **488**, 31–78.
- MA, Y. & ZHONG, X. 2003b Receptivity of a supersonic boundary layer over a flat plate. Part 2. Receptivity to free-stream sound. *J. Fluid Mech.* **488**, 79–121.
- MA, Y. & ZHONG, X. 2003c Receptivity to free-stream disturbances of Mach 8 flow over a sharp wedge. *AIAA Paper* 2003-0788.
- MACK, L. M. 1984 Boundary layer linear stability theory. *AGARD Rep.* **709**, pp. 3-1–3-81.
- MACK, L. M. 1987 Stability of axisymmetric boundary layers on sharp cones at hypersonic Mach numbers. *AIAA Paper* 87-1413.
- MCKENZIE, J. F. & WESTPHAL, K. O. 1968 Interaction of linear waves with oblique shock waves. *Phys. Fluids* **11**, 2350–2362.
- MALIK, M. R. 1990 Numerical methods for hypersonic boundary layer stability. *J. Comput. Phys.* **86**, 376–413.
- MALIK, M. R., SPALL, R.E. & CHANG C.-L. 1990 Effect of nose bluntness on boundary layer stability and transition. *AIAA Paper* 90-0112.
- MASLOV, A. A., MIRONOV, S. G. & SHIPLYUK, A. A. 2002 Hypersonic flow stability experiments. *AIAA Paper* 2002-0153.
- MASLOV, A. A., SHIPLYUK, A. N., SIDORENKO, A. & ARNAL D. 2001 Leading-edge receptivity of a hypersonic boundary layer on a flat plate. *J. Fluid Mech.* **426**, 73–94.
- MORKOVIN, M. V. 1987 Transition at hypersonic speeds. *ICASE Interim Report 1*, NASA CR 178315.
- POTTER, J. L. & WHITFIELD, J. D. 1962 Effects of slight nose bluntness and roughness on boundary-layer transition in supersonic flows. *J. Fluid Mech.* **12**, 501–535.
- RESHOTKO, E. 1991 Hypersonic stability and transition. In *Hypersonic Flows for Reentry Problems* (ed. J.-A. Desideri, R. Glowinski & J. Periaux), **1**, 18–34. Springer.
- SARIC, W. S., REED, H. L. & KERSCHEN, E. J. 2002 Boundary-layer receptivity to free-stream disturbances. *Annu. Rev. Fluid Mech.* **34**, 291–319.
- SCHNEIDER, S. P. 2001 Hypersonic laminar instability on round cones near zero angle of attack. *AIAA Paper* 2001-0206.
- STETSON, K. F. & KIMMEL, R. L. 1992 On hypersonic boundary layer stability. *AIAA Paper* 92-0737.
- STETSON, K. F. & KIMMEL, R. 1993 On the breakdown of a hypersonic laminar boundary layer. *AIAA Paper* 93-0896.
- STETSON, K. F., THOMPSON, E. R., DONALDSON, J. C. & SILER, L. G. 1984 Laminar boundary layer stability experiments on a cone at Mach 8. Part 2: Blunt cone. *AIAA Paper* 84-0006.
- ZHONG, X. 1997a Direct numerical simulation of hypersonic boundary-layer transition over blunt leading edges. Part II: Receptivity to sound (invited). *AIAA Paper* 97-0756.
- ZHONG, X. 1997b Direct numerical simulation of hypersonic boundary-layer transition over blunt leading edges, Part I: New numerical methods and validation (Invited). 35th AIAA Aerospace Sciences Meeting and Exhibit, January 6–9, Reno, Nevada. *AIAA Paper* 97-0755.

- ZHONG, X. 1998 High-order finite-difference schemes for numerical simulation of hypersonic boundary-layer transition. *J. Comput. Phys.* **144**, 662–709.
- ZHONG, X. 2001 Leading-edge receptivity to free stream disturbance waves for hypersonic flow over a parabola. *J. Fluid Mech.* **441**, 315–367.
- ZHONG, X. & TATINENI, M. 2001 Stable high-order schemes and DNS of boundary-layer stability on a blunt cone at Mach 8. *AIAA Paper* 2001-0437.